

EVALUATION OF LOCAL FIELD POTENTIALS AND INFLAMMATORY RESPONSE TO  
CHRONIC MICROELECTRODE ARRAYS IN RAT MOTOR CORTEX

by

Ellen Shih

APPROVED BY SUPERVISORY COMMITTEE:

---

Stuart F. Cogan, Chair

---

Joseph J. Pancrazio

---

Heather N. Hayenga

---

Danieli C. Rodrigues

Copyright 2018

Ellen Shih

All Rights Reserved

“And we are led  
To those who help us most to grow  
If we let them”  
- Wicked

EVALUATION OF LOCAL FIELD POTENTIALS AND INFLAMMATORY RESPONSE TO  
CHRONIC MICROELECTRODE ARRAYS IN RAT MOTOR CORTEX

by

ELLEN SHIH, BS

THESIS

Presented to the Faculty of  
The University of Texas at Dallas  
in Partial Fulfillment  
of the Requirements  
for the Degree of

MASTER OF SCIENCE IN  
BIOMEDICAL ENGINEERING

THE UNIVERSITY OF TEXAS AT DALLAS

December 2018

## ACKNOWLEDGMENTS

I would like to thank the many people who invested their time and effort into my education.

I thank Dr. Stuart Cogan, without whom this opportunity would not have been possible. Offering me a place in his lab has opened my mind to limitless opportunities. Dr. Aswini Kanneganti was a consummate mentor, there for every hesitant step of the way. Dr. Alexandra Joshe-Imre offered me invaluable feedback and helped me develop my ideas.

I extend my gratitude to Dr. Joseph Pancrazio and Dr. Mario Romero-Ortega, for their guidance and advice in my projects.

I am thankful for the kind patience of Dr. Heather Hayenga and Dr. Danieli Rodrigues in their efforts as members of my committee.

To the members of the NIL, NNIL, and RNN labs who make up the conglomerate along the south side of the 3<sup>rd</sup> floor, it was enough that you were there.

The author looks back fondly on her time among these wonderfully brilliant and generous people.

August 2018

EVALUATION OF LOCAL FIELD POTENTIALS AND INFLAMMATORY RESPONSE TO  
CHRONIC MICROELECTRODE ARRAYS IN RAT MOTOR CORTEX

Ellen Shih, MS  
The University of Texas at Dallas, 2018

Supervising Professor: Stuart F. Cogan, Chair

Neural interface devices are being developed for applications encompassing communication interfaces between prosthetics and patients and investigative tools for understanding complex neural circuitry. This work investigates encapsulation materials and strategies for chronic recording of neural electrical signals for intracortical electrodes. These devices could be used for brain-computer interfacing in applications related to the recording of volitional intent in conditions such as brainstem stroke, spinal cord injury, and locked-in syndrome. Intracortical microelectrode arrays (MEAs), such as the Utah-style electrode array (UEA) which is currently in clinical trials for neural recording in brain-computer interfacing, suffer from a lack of chronic reliability. A number of abiotic and biotic factors have been identified as contributors to the decline in performance. The primary biotic mechanism for loss of device performance is associated with the inflammatory response that follows implantation and chronic residence in the brain parenchyma. This foreign body response is characterized by glial scarring, loss of viable neurons, and persistent astrogliosis. A significant abiotic failure mechanism involves loss of integrity of polymer encapsulation coatings that may delaminate or become ineffective as barrier coatings resulting in

parasitic electrical leakage pathways and corrosion. How adverse tissue reaction and material failure in MEAs interact and affect device performance is yet to be fully understood.

This thesis investigates two elements of the chronic performance of neural interfaces: 1) the use of local field potentials (LFPs) as an alternative to single-units as a quantification of recording performance of cortical interfaces, and 2) the adverse foreign body response to amorphous silicon carbide (a-SiC), as an alternative encapsulation material for intracortical devices.

The performance of neural electrodes is typically quantified by the capability of the device to measure neuron single-unit activity. However, single-unit activity is challenging to use as a volitional control signal due to an observed variability of recorded action potentials at electrodes during chronic studies. It is known that LFPs represent the sum of the low frequency (<300 Hz) electrical activity surrounding an electrode, and have drawn interest as a signal for brain-computer-interface control. However, the long-term stability of LFPs is less well-established. We describe a method of evaluating the trends in LFPs over time and show they reflect the decline in performance as shown by single-unit activity. We identify a time window in which the decline is most prominent, which also correlates with changes in the longitudinal electrochemical properties of the recording electrodes measured in vivo in the same animal preparations.

Towards the second goal, we aim to minimize the immune response to intracortical devices. It is known that some encapsulation materials for intracortical devices on the market are not optimal. For example, the current Utah-style MEAs employ Parylene-C, a poly(xylylene) polymer, as an encapsulation material.. This material has been documented to delaminate and therefore result in leakage and shunting of current, reduced signal-to-noise ratio of neural data, and corrosion.

Additionally, biocompatibility of the encapsulation influences the extent of the foreign body

response. Amorphous SiC is a material with several desirable electrical and material properties as an encapsulation for implanted MEAs, including high electrical resistivity, a low bio-reactivity, and extremely low dissolution rate. We compare the foreign body response to a-SiC and Parylene-C encapsulated arrays implanted in rat cortical tissue through progressive histochemical analysis. Our results show that Parylene-C shows a reduced inflammatory response compared to a-SiC or bare Si over a period of 120 days as measured by the spatial distribution of reactive astrocytes, microglial and neurons around implanted electrodes. This thesis discusses alternative methods of evaluating cortical electrode performance and offers insight into a different encapsulation material.



## TABLE OF CONTENTS

ACKNOWLEDGMENTS .....	v
ABSTRACT.....	vi
LIST OF FIGURES .....	x
LIST OF TABLES.....	xiii
CHAPTER 1 INTRODUCTION .....	1
1.1 Neural Electrodes.....	2
1.2 Chronic stability.....	4
1.3 Chronic Failure .....	5
1.4 Justification.....	7
1.5 Organization.....	9
CHAPTER 2 LOCAL FIELD POTENTIALS AS A MEASURE OF UTAH ELECTRODE ARRAY PERFORMANCE .....	10
2.1 Introduction.....	10
2.2 Methods.....	13
2.3 Results.....	16
2.4 Discussion.....	21
CHAPTER 3 A HISTOLOGICAL COMPARISON OF CHRONICALLY IMPLANTED AMORPHOUS SILICON CARBIDE AND PARYLENE-C-COATED UTAH ELECTRODE ARRAYS IN RAT CORTEX .....	26
3.1 Introduction.....	26
3.2 Methods.....	30
3.3 Results .....	34
3.4 Discussion.....	40
CHAPTER 4 CONCLUSION.....	46
REFERENCES .....	49
BIOGRAPHICAL SKETCH .....	59
CURRICULUM VITAE .....	

## LIST OF FIGURES

Figure 1: 4x4 UEA used for implant in rat cortex. Electrode pitch (distance from one electrode to the next) measures 400 $\mu\text{m}$ . Shank length measures 1 mm. ....	3
Figure 2: Representative LFP band power to Week 26. Array 3 remained functional until the end of the study, while Array 10 stopped reporting single units from Week 10 onwards. (A) Band power in delta (0-4 Hz), theta (4-8 Hz), alpha (8-14 Hz), beta (14-30 Hz) and gamma (30-100 Hz) bands. (B) EIS of Array 3 shows minimal change pre- and post-implant. (C) EIS of Array 10 is greatly changed between pre- and post-implant in vitro measurements.....	18
Figure 3: Heat map of bandpower shows changes from week to week on a logarithmic scale. Spontaneous activity is primarily in the 0-8 Hz range, with weaker changes visible between 8-100Hz.....	19
Figure 4: Bandpower vs RMS potential (A) and total # of single units (B). Strong correlation between bandpower and both measures ( $R= 0.95, 0.67$ respectively). Measures decline gradually, reaching a stable low level around weeks 16-17. ....	20
Figure 5: LFP bandpower decline is not correlated with impedance at 1kHz (A), 1Hz (B) or 100Hz (C). $R = 0.22, 0.36, 0.03$ from A-C.....	21
Figure 6: Bandpower in Working vs Non-Working arrays. Linear fit slopes were not significantly different, suggesting there is some cause of gradual decline in performance unrelated to wire bundle breakage reported in Non-Working arrays. ....	22
Figure 7: Relationship between Spike and LFP signals. Representative segment from Array 3, Week 12. Spike bursts coincide with large-amplitude LFPs. ....	23
Figure 8: Bandpower over time, in the presence (A) or absence (B) of a single unit recorded on the channel. Points in blue (X-1,3,6,7) came from animals not exhibiting wire breakage. Points in red (*-4,8,9,10) came from arrays with wire breakage. Array 5 (+) showed wire breakage by Week 19 but reported very low bandpower.....	24
Figure 9: Array 5. (A) An exception to either rule, LFP bandpower was persistently low regardless of the presence or absence of identified single units. (B) Large change between initial and explanted impedance spectra is characteristic of wire bundle breakage.....	25
Figure 10: UEA with silicone backside encapsulation. Mark on backside (a) to indicate array orientation. (b) 4x4 grid of electrode shanks with 400 $\mu\text{m}$ pitch and 1 mm length. ....	30

Figure 11: Bilateral craniotomy and implant of UEA. (a) Placement of craniotomy and screws relative to cranial sutures. (b) Untethered UEA resting on brain prior to insertion. (c) Bilateral insertion of UEAs, covered with collagen-based dura graft. (d) Craniotomy sealed with medical-grade silicone and bone cement anchored to screws. (e) Blood vessels at implant site, typically present. ....31

Figure 12: Custom program for image quantification. Composite images for each array were imported into MATLAB, and electrode locations were manually defined. Concentric bands were defined from each electrode. Intensity of CD68 and GFAP expression were calculated automatically in 5  $\mu\text{m}$  bands, while neurons were manually counted in 25  $\mu\text{m}$  bands, to a maximum of 250 $\mu\text{m}$  from the electrode. (a) NeuN. (b) CD68. (c) GFAP. ....34

Figure 13: Cranial bleeding caused premature death. Array geometry causes significant vascular damage in rat. (a) Subcutaneous hematoma. (b) Bleeding evident beneath bone cement around right craniotomy. (c,d) Remnants of severe bleeding seen from inside the skull. .35

Figure 14: SEM images of arrays showing fibrous and cellular adherents following explant. (a,b,c) Unspecified cell adherents on the surface of the array. (d) RBCs. ....35

Figure 15: UEA explant. Optical photographs showing typical (a-c, e-g) and atypical (d,h,i) array and tissue condition. Residue from bleeding can be seen in on both the array (b) and tissue (f,g,h). Lesion severity ranged from mild (f) to severe (e), eliminating any trace of individual electrode shanks. ....36

Figure 16: Representative images as compared to no primary antibody controls. Controls showed minimal nonspecific binding and served as a value for normalization. ....38

Figure 17: Normalized neuronal density per unit area  $\pm$  SEM as a function of distance from the edge of the electrode across all shanks in arrays. \*Parylene-C density is significantly higher ( $P < 0.0001$ ) than a-SiC at all distances and time points. ....39

Figure 18: Normalized GFAP fluorescence intensity  $\pm$  SEM as a function of distance from electrode hole edge. There was a noticeable difference in response within a radius of 30  $\mu\text{m}$ , after which the presence of astrocytes was fairly uniform. Difference between materials was most significant at 60 and 120 days ( $P < 0.0001$ ). ....40

Figure 19: Normalized fluorescence intensity  $\pm$  SEM of CD68 as a function of distance. The difference between Parylene-C and a-SiC was significant within a small radius of the electrode. ....40

Figure 20: Absence of electrode perforations as a result of lesion. (a) Error in implant placed device at an angle, and collagenous adhesions are visible on the surface of the array. (b) Large lesion and discoloration in the surface of the brain, as well as the absence of clear electrode

holes. (c) Edges showed a mixture of CD68 and GFAP expression, but few recognizable cell bodies. ....41

Figure 21: Discrepancies in electrode perforation size at a nominal slice depth. (a) Different size electrode holes in a single slice shows a skewed plane of slicing. (b) Electrode size across all assessed samples with at least 1 definitive electrode hole. Radius 0 indicates the absence of an electrode hole. (c) Explant reveals implant is not certain to be flush to the surface of the brain, and therefore not at a consistent depth.....43

Figure 22: Discoloration of unstained tissue surface (A) corresponds to large areas of fluorescent antibody binding in all channels. (B) shows superimposed fluorescent staining of highlighted region from NeuN (C, blue), CD68 (D, green) and GFAP (E, red). .....44

Figure 23: Intra-array electrode variability. Expression of CD68 (green) and GFAP (red) were highly concentrated in one section of the array in the lower right.....45

## LIST OF TABLES

- Table 1: Experimental Groups. Animals were bilaterally implanted with arrays in the somatosensory cortex. A total of 54 devices (n=6) was implanted in 27 animals.....32
- Table 2: Gross histology overview, based on typical outcomes described in Figure 15. There was no correlation between encapsulation or implant duration and outcomes. ASC = amorphous silicon carbide. BSI = bare silicon. PLC = Parylene-C. ....37

# CHAPTER 1

## INTRODUCTION

One of the primary motivations in the development of neural interfaces is to assist the thousands of people with physical disabilities due to spinal cord injuries, amyotrophic lateral sclerosis, and other diseases or injuries of the nervous system [1]. These conditions severely hamper their ability to interact with their environment or live independently, and are costly in both additional healthcare expenses and lost opportunities. Data from 2011 estimates the lifetime healthcare cost of tetraplegia to be as much as \$4.7 million [1]. Treatment for these conditions is challenging, due to the limited capability of the central nervous system to regenerate [2]. Assistive devices such as conventional passive prosthetics and physical rehabilitation aid in the recovery of only limited basic functions, which is among the reasons patients abandon treatment [3]–[5]. Alternatively, active prosthetics, which allow for greater user interaction and functionality, are slow and cumbersome. They operate with myoelectric signals, which require residual muscle control and do not provide feedback. For conditions such as tetraplegia and locked-in-syndrome, eye- and head-tracking systems allow patients to interact with communication interfaces.

Brain-computer interfaces (BCIs) are gaining popularity as a strong alternative strategy for assistive devices in circumstances where cortical and cerebellar structures are largely intact, as in spinal cord and brainstem injuries. Neural control methods promise to be a more intuitive and flexible solution for prostheses and other assistive devices, offering more detailed input and feedback data [6], [7]. Many animal [8]–[14] and humans [15]–[19] feasibility studies have already shown the possibilities for this technology.

The field of neural devices encompasses a broad spectrum of applications and device technology for interfacing with the nervous system. Neural devices can be non-invasive or implanted, and placed in both the central and peripheral nervous systems. They have been crucial to expanding the understanding of neural circuitry, seeing use in the stimulation and recording of in vivo and in vitro neural tissue. From the simplest of EEG-driven systems to implantable ECoG and penetrating electrode devices with resolution for both stimulation and recording orders of magnitude greater, brain-computer interfaces (BCIs) promise a vastly improved quality of life for people suffering from injuries or disease that limit their ability to interact with their environment. Although neural signals are far from being fully understood, BCIs have already found success in augmenting the lives of people suffering from tetraplegia and locked-in syndrome [17], [19], [20].

### **1.1 Neural Electrodes**

The past decade has seen many advances in the design and development of implantable neural electrodes for use in the brain. Different designs, fabrication methods, and materials for electrodes and encapsulation have been explored to variable effect [21], [22]. The high vascularity of the central nervous structures and relative fragility inform the type of electrode used. While surface electrodes cause less damage to tissue during implantation [23], [24], intracortical electrodes offer greater selectivity and efficiency by virtue of their closer proximity to neurons [25], [26]. The reduced electrode-neuron distance allows intracortical electrodes to use lower currents to stimulate neural activity and likely with fewer side effects from off-target stimulation.

Of particular interest to BCIs are intracortical multi-electrode arrays (MEAs), which incorporate increasingly large numbers of recording sites in micro-scale intraneural electrodes

using commercial microfabrication techniques. Higher electrode densities allow for greater spatial specificity, which is highly desirable in cortical gray matter applications. Intracortical electrodes have been the subject of multiple acute and chronic studies for both stimulation and recording. Of the handful of MEAs capable of single-unit recordings that have proven functionality in animal trials, very few have made it into clinical trials.

### 1.1.1 Utah Electrode Array

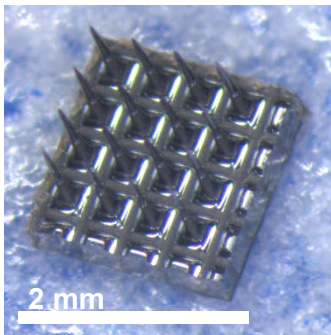


Figure 1: 4x4 UEA used for implant in rat cortex. Electrode pitch (distance from one electrode to the next) measures 400  $\mu\text{m}$ . Shank length measures 1 mm.

The Utah electrode array (UEA) is one of the very few intracortical MEAs used in clinical applications, being the device of choice for the ground-breaking BrainGate pilot studies and epilepsy research [27]. It is composed of rigid silicon, machined into pyramidal electrodes from a monolithic substrate and coated with an insulating dielectric and conductive tip. Compared to other MEAs, the UEA covers a large planar area, being composed of an array of evenly spaced singular electrodes rather than multiple electrode sites along the length of a shaft (Figure 1). This allows the array to “self-anchor” [28] which makes for more stable recordings. Electrodes may be at a uniform depth, as in the classic UEA, or at multiple depths, in the case of the slanted UEA which is used in peripheral nerve applications.



The performance and stability of the UEA for stimulation and recording has been the subject of multiple animal studies in both acute and chronic experiments. Early success in preclinical studies in feline [29] and non-human primate [30]–[32] preparations prompted the swift advancement to investigational use in humans [15]–[18], [20], as well as additional work exploring design iterations [33] and implantation techniques [34], [35]. While decoding and encoding of neural activity is still largely a mystery, the long-term functionality of the UEA has been tested in multiple studies, reporting stability for periods of a few months [36] to a beyond a year [16] in different animal models and human subjects.

## **1.2 Chronic stability**

The long-term viability of neural electrodes is still to be demonstrated. The immune response in the central nervous system, which results in glial scarring and a neurotoxic environment, and the spatial resolution required of BCI applications, add to the need for neural devices with long-term chronic reliability. An important measure of microelectrode device functionality is the ability to record single-neuron origin action potentials, quantified as single units (SUs). SUs are extracted from filtered neural recordings by means of spike sorting algorithms that attempt to identify spiking activity from a single neuron. However, over longer periods of time, these methods do not account for similar waveforms from multiple neurons [37] or changes to waveforms from a single neuron [38].

### **1.2.1 Local Field potentials**

Field potentials measure the flow of currents generated by ionic electrical activity of large populations of neurons in the brain. They can be measured non-invasively with electroencephalography, or invasively using electrocorticography, and are limited to low frequency and spatial resolution. Intracortical microelectrodes measure field potentials on a smaller scale than either method, though the extent of that localization is still debated [39]. LFPs have successfully been used for signal-decoding in BCIs [20], [32], [40] using intracortical electrodes.

## **1.3 Chronic Failure**

A host of abiotic and biotic factors contribute to the failure of MEAs, but these factors are difficult to definitively discern *in vivo*. The decline in performance for chronic implants is well-documented [16], [31], [41]–[44], typically defined by the loss of measureable action potentials. This can be a result of mechanical damage to the array or connecting hardware, or more gradual as a result of material flaws or biological response [45]–[51]. Most of these interactions are difficult to simulate outside the body, and cannot be directly measured *in vivo*.

### **1.3.1 Abiotic Failure Mechanisms**

Physical changes to the array materials such as delamination or cracking of either encapsulation, electrode material, or other insulation cause noticeable electrical changes, including changes to impedance and signal quality. Materials are susceptible to defects in fabrication, which are compounded by film stresses, chemical changes, and reactive species generated by the foreign

body response. Residual stresses from fabrication or poor adhesion may cause delamination or cracking in insulation or conductive materials. The resulting damage can be observed using imaging techniques such as scanning electron microscopy, while stress can be calculated using techniques such as nano-indentation or x-ray diffraction [52], but these methods are ill-suited to the geometry of the UEA. Electrochemical characterization such as voltage transient measurements, impedance spectroscopy, and cyclic voltammetry can be used to observe changes in charge transfer capacity and resistivity to implanted electrodes and in some circumstances identify material failure mechanisms. For stimulation applications, the charging behavior of electrodes is useful in establishing the parameters for stimulus delivery. Impedance affects the efficiency of stimulation and signal-to-noise ratio of recording applications [53].

### **1.3.2 Biotic Failure Mechanisms**

Biotic changes at the implant site disrupt the array as a result of the inflammatory response, vascular damage, and activation of glial cells. Meningeal proliferation, glial scarring, and neuronal cell loss have all been suggested as possible causes of signal loss [34], [51], [54]. Immediately following implantation, broken vasculature releases inflammatory cytokines, which activate an initial cascade of immune cells and additional signaling molecules leading to effects similar to hemorrhagic stroke. The presence of the implant may perpetuate the inflammatory response resulting in persistent reaction to the implant. Most biotic changes cannot be observed without extracting the array and performing a histological assessment of the cellular types and spatial distribution at the implant site. Immunohistochemistry, an effective means of quantifying the proliferation and migration of astrocytes and microglia to the implanted device, as well as the

changes to neuronal density, is typically used for the histological assessment. While the physiological response to chronic indwelling electrodes is well-documented, the connection between resultant changes to brain tissue and electrode function is poorly understood.

#### **1.4 Justification**

Device lifetime is a crucial element for the advancement of neural electrodes beyond the research laboratory. Potential brain-computer interface applications for neural electrodes extend to many physical disabilities, and have already shown promise in clinical trials translating volitional intent into control signals. However, the decline in performance and eventual failure of devices requires further research.

Current methods of measuring electrode recording performance are limited primarily to the use of single units and are also confounded by several abiotic and biotic factors whose complex interactions lead to device failure. Alternative approaches looking at changes in electrochemical properties to investigate the chronic functionality and performance have been explored, but these techniques are time consuming and require additional instrumentation, limiting their use for chronic experimentation. Spontaneous LFP stability is another alternative to single units that is gaining traction. We propose to investigate spontaneous LFPs as a potential informative and easily implemented method of assessing electrode function in chronic implants.

Equally important for stable chronic performance in the UEA is the integrity of the encapsulation layer. Conventional UEAs are insulated with Parylene-C, a well-tolerated and stable polymer that produces conformal coatings [55]. However, Parylene-C cracking has been observed

in chronic in vivo studies and has been associated with a decline in single-unit neural recording performance [41]. The cracking has been attributed to a mixture of residual stress and reactive oxygen species, but has not been reproduced in ex vivo studies. We, among others, have been exploring amorphous silicon carbide (a-SiC) as an insulating material for intracortical devices [56]–[58]. To this end, our second aim is to compare the chronic histological response to a-SiC and Parylene-C on UEAs.

Taken together, the hypotheses developed are:

1. LFP stability over time will be useful measure for quantifying the recording capabilities of neural electrodes in the absence of identifiable single-unit activity.
2. Amorphous silicon carbide will be tolerated by the brain immune response for use as an electrode coating for UEAs.

The first hypothesis is addressed by implanting 10 rats with UEAs and tracking the weekly recorded spontaneous LFP's under anesthesia from the motor cortex over a 6-month period. Additionally, the electrochemical properties of the implanted electrodes will be measured in parallel with LFP measurements in an effort to identify possible reasons for observed changes in spontaneous LFP activity.

For the second hypothesis, we have implanted 27 rats bilaterally in the somatosensory cortex with UEAs encapsulated with Parylene-C and a-SiC, using uncoated silicon as a positive control. Time points of 60, 90, and 120 days post-implantation were selected for the study. Existing comparisons of these materials have analyzed neural implant histology to a maximum of 84 days

(12 weeks) [59], [60]. At each time point, arrays were extracted for scanning electron microscopy, and brains were prepared for immunohistochemical comparison of astrocyte, microglial, and neuronal expression.

## **1.5 Organization**

This thesis discusses the chronic performance and failure of neural interface devices, focusing on encapsulation materials and strategies for chronic recording of neural electrical signals for devices that could be used for brain-computer interfacing in applications related to the recording of volitional intent in conditions such as brainstem stroke, spinal cord injury, and locked-in syndrome. The first chapter briefly introduces methods, measurements, and mechanisms of chronically evaluating neural devices. The remainder of this thesis is as follows:

Chapter 2 analyzes local field potentials recorded by functional UEAs in rat cortex over the course of 30 weeks, comparing power spectra with concurrent signal analysis methods and electrochemical characterizations to determine their utility as a measure of performance.

Chapter 3 compares the outcomes of a novel UEA coating, amorphous silicon carbide (a-SiC), to the conventional Parylene-C using immunohistochemical measures.

Chapter 4 concludes the thesis with a summary of the findings with respect to current understanding of the chronic effects of neural devices in the brain.

## CHAPTER 2

### LOCAL FIELD POTENTIALS AS A MEASURE OF UTAH ELECTRODE ARRAY

#### PERFORMANCE

Animal data and single-unit analysis for this study was provided by Dr. Bryan Black and published in the Journal of Neurophysiology [61]. Surgeries were performed by Dr. Bryan Black, Dr. Aswini Kanneganti, and Dr. Chris Frewin. Data collection was performed by several members of the Neural Interfaces and Neural Networks Labs. Local field potential data analysis was conducted by the author.

#### 2.1 Introduction

By identifying patterns in brain activity, BCI algorithms can translate neural field potentials into control signals for prostheses, assistive devices, and computers. These algorithms use varied signals sources to mixed success, limited by current state of machine learning, recording capabilities, and understanding of neural circuitry [62].

Early neural BCI work in the 1970's analyzed field potentials acquired by electroencephalography (EEG), using spectral analyses and temporal cues to identify components of interest [19], [63]–[65]. Signals from mu (8-12 Hz) and beta (18-26 Hz) frequency bands associated with movement are measured and compared to a threshold. With a few months of training and feedback [66], patients are able to control the amplitude of oscillations. Steady-state visual evoked potentials (SSVEPs) are another well-researched method of generating BCI input, using characteristic signals triggered by blinking lights. Systems utilizing visual evoked potentials require less training and produce swifter, more variable output but suffer from high rates of false

positives [67]. Another problem with EEG-based BCIs is the large amount of noise due to non-neural tissue between the electrode and brain [63], [65]. Some success has been found for the use of electrocorticography (ECoG) to drive BCI input in acute experiments [68], [69]. Measured with flexible surface multielectrodes (MEAs) placed on the subdural brain surface, ECoG is less susceptible to noise artifacts and is capable of greater spatial and temporal resolution.

Intracortical microelectrodes have far outpaced the recording capabilities of EEG and ECoG [70]. Microelectrodes are capable of interacting with very small volumes of tissue deeper in the cortex and at high frequencies, allowing for the measurement and mapping of single-neuron action potentials. With more detailed signals, the hope is to identify specific features for volitional movement to control more advanced prostheses. Several non-human primate studies have reported on the use of intracortical electrodes in identifying reach and gaze kinematics encoded by neural signals [37], [71]–[75]. Neurotrophic cone electrodes implanted in human patients were used by Kennedy in the late 1990s to operate a communication software cursor [76]–[78], analyzing increases in a single cell’s firing rate. The first and second BrainGate pilot trials use the Utah Electrode Array (UEA) to great effect in assisting tetraplegic and otherwise severely physically disabled patients [15]–[17], [20], [79]. Researchers successfully recorded from an ensemble of neurons and designed a control scheme using spike rates to operate cursor interfaces and robotic devices [15], [17]. Arrays remained functional beyond 1000 days, but experienced at least partial failure in individual electrodes, which was determined by abnormally high impedance measurements and a failure to detect units.

The primary method of quantifying electrode performance is the measurement of single units, which are action potentials that can be identified as coming from the same neuron based on



sorting algorithms. Extracting single units from multiunit recordings requires a number of assumptions, chiefly that action potential waveforms are consistent and unique to the source cell [38]. This does not account for neurons with similar waveforms or changes to the waveform over the course of multiple recording sessions [80], making single unit quantity or consistency fallible measures of stability [37]. Another consideration for measurements conducted under anesthesia is the effect various anesthetics have on firing rate[81]–[83]. These problems with single units have also driven interest in alternative control signals for BCIs.

### **2.1.1 Local Field Potentials**

Local field potentials (LFPs) in the brain reflect the extracted low frequency (<300Hz) shifts in electrical potential of the extracellular space surrounding an electrode. These shifts are the accumulation of ionic current sources and sinks caused not only by cell firing, but inhibitory and subthreshold currents as well [84]. The scale on which local field potentials are local is not well defined, and varies according to the size of the electrode, as well as tissue conduction and signal frequency [39]. It is not clear what activity can be extracted from LFP oscillations, but the common consensus is that they reflect the behavior of ensembles of neurons. Most analysis subdivides LFPs into narrower frequency bands [85]–[87], looking for features of interest. These bands can be subjective but typically correspond to ranges established by EEG and field potential research: delta (0-4 Hz), theta (4-7 Hz), alpha or mu (8-12 Hz), beta (12-30 Hz), and gamma (30-100+ Hz) [88]. These bands are primarily associated with certain kinds of activity or resting states, but may also encode other neural behavior. Although LFPs are filtered from the low frequency

spectra of broadband recordings, there remains evidence that they reflect high-frequency spiking activity either by genuine connections or contamination [89]–[93].

Despite these uncertainties, local field potentials have also found interest as a feedback element of closed-loop control for deep brain stimulation (DBS) in the treatment of Parkinsonian symptoms [94]–[98]. The macroelectrodes used for DBS have recorded beta frequency (13-30Hz) oscillations in the basal ganglia or thalamic targets, coinciding with tremor or rigidity that was suppressed by treatment [96]. Other work with LFPs focus on signal encoding for use in BCIs, evoked by volitional intent [20], [99]. In comparison with spike data, LFPs have been found to perform comparably to spikes, sometimes better and sometimes worse [40]. LFPs may also exist independently of spike activity [16], [100], incentivizing their use as a control signal for BCIs.

With this growing interest in LFPs, we find it of value to investigate the chronic stability of LFP signals. In the absence of evoked activity, we expect spontaneous LFPs to reflect the passive performance of the electrode with a minimum of conflating variables.

## **2.2 Methods**

### **2.2.1 Animal Procedures**

All procedures were performed under protocols approved by the University of Texas at Dallas Institutional Animal Care and Use Committee. Surgery and recordings were performed as described by Black et al. [61]. In brief, rats were surgically implanted with a 16-channel UEA with 1mm long electrode shanks, Parylene-C encapsulation, SIROF tips, and 2.5 cm (n=5) or 5cm (n=5)

wire bundle lengths leading to an Omnetics- connector (Blackrock Microsystems, Salt Lake City, UT) in the right motor cortex.

Adult male Long-Evans rats (330-380g) were anesthetized with intraperitoneal injection of ketamine (65 mg/ kg) xylazine (13.33 mg/kg) acepromazine (1.5 mg/kg) cocktail. Surgical-depth anesthesia was maintained with isoflurane mixed with 100% O<sub>2</sub>. Rectal temperature, heart rate, and blood pressure were monitored the duration of surgery. Animals were shaved and positioned on a stereotaxic frame. Local anesthetic (lidocaine) was injected along the midline prior to a single primary incision from between the eyes to between the ears. The skull was exposed and a rough 2mm x 2mm square craniotomy opened above the right motor cortex. Three support screws were placed in the remaining quadrants of the skull, 1 opposite across the midline from the craniotomy and the other 2 opposite across the bregma. Care was taken during drilling to prevent tissue heating by applying saline rinses.

The dura mater was reflected and the UEA inserted at 1m/s with a pneumatic inserter (Blackrock Microsystems, USA). The craniotomy was covered with a collagen-based dural graft (Biodesign Dural Graft, Cook Medical, USA), followed by a silicone elastomer gel (Kwik-Cast, WPI, USA). Platinum ground and reference wires were wrapped around two bone screws. When the elastomer cured, dental bone cement was used to form the heat cap, sealing the craniotomy, bone screws, and Omnetics connector. The skin was closed around the percutaneous connector with surgical staples, and the animal was allowed to recover.

## 2.2.2 Single Unit and LFP Recordings

In vivo neural recordings were collected once per week, beginning one week post-implant. Animals were lightly anesthetized under 1.7% isoflurane and connected externally via a HST/16D Gen2 16 channel head stage to the Digital Headstage Processor (Plexon, USA) for analog-to-digital conversion. Wide band data (0.1 – 7000 Hz) were collected from all 16 recording electrodes simultaneously at 40,000 Hz sampling rate for 10 minutes using the Plexon's Omniplex chassis and Plexon PlexControl software.

For single unit detection and discrimination, wide band data was band-pass filtered (250 – 7000 Hz) using a 4-pole Butterworth filter and a threshold was set at  $4\sigma$  based on RMS noise. Single units were manually sorted based on amplitude and principal component space analysis. SNR was calculated as

$$\text{SNR} = \frac{\text{Signal}}{\text{RMS}_{\text{Noise}}}$$

where  $\text{RMS}_{\text{Noise}}$  was calculated from the entire filtered continuous recording. Additional processing and analysis was carried out using Plexon's Offline Sorter, NeuroExplorer (Nex Technologies, USA) software, and a custom MATLAB script.

LFP data was extracted from wide band data with a 2<sup>nd</sup> order Butterworth bandpass (0.1-300 Hz) filter. Recordings were cut to a uniform length and analyzed in MATLAB (Mathworks, Natick, MA) using custom and in-built functions in the Signal Processing Toolbox. The `pwelch` function was used to calculate the Welch's power spectral density with a 2 second Hamming window and 50% overlap. Power in the band was calculated with the `bandpower` function, taking the integral of the power spectral density estimate over frequency ranges corresponding to bands

of interest from the literature (Delta: 0-4 Hz, Theta: 4-8 Hz, Alpha/Mu: 8-14 Hz, Beta: 14-30 Hz, and Gamma: 30-100 Hz).

A baseline noise value was determined by conducting a recording with a non-implanted array placed in a beaker of saline.

### **2.2.3 Electrochemistry**

Electrochemical measurements were performed with a GAMRY Reference 600 potentiostat in a three-electrode configuration (working, counter, and reference). In vitro measurements were performed in an inorganic model of interstitial fluid (ISF) at 37°C [101]. In vivo measurements utilized an external reference (chloridized silver wire) and counter (platinum wire) electrodes secured to the animal's tail and wrapped in PBS saturated gauze to maintain conductive contact.

Cyclic voltammetry was conducted between limits of -0.60 V and 0.80 V versus Ag|AgCl at sweep rates of 50 mV/s and 50,000 mV/s. The charge storage capacity was calculated from the third of three consecutive CV cycles using methods described previously [102].

Impedance spectroscopy (EIS) measurements were made at measured open-circuit potential using a sinusoidal 10mV RMS excitation over a range of  $10^0$  to  $10^5$  Hz at 10 points per decade.

## **2.3 Results**

In vivo neural recordings and electrochemical measurements were taken weekly beginning one week post-implant until the 6-month endpoint. Of the 10 implanted animals, 3 did not reach

the terminal date; one suffered mechanical detachment of the head cap (Array 2, 28 days post-implant) and two expired of unknown causes (154 and 162 days post-implant). Animals were excluded from a week's measurements on the grounds of complications with the head cap or connection. For this analysis, we only report data up to 26 weeks, after which the difference week-to-week was negligible. Data was averaged across all 16 electrodes on the array. Array 2 was exempted from analysis, due to the short duration of the implant.

Figure 2A shows the trend in bandpower in two representative arrays over the course of 26 weeks. Array 3 continued to report single units the study endpoint, while Array 10 experienced a sudden absence of units beginning week 10 until the end of the study. Upon the sudden and persistent absence of units, bandpower fell to values comparable with the saline noise baseline (not pictured,  $9.67 \text{ e-}6 \pm 0.005 \text{ e-}6 \text{ a.u.}$ , mean  $\pm$  SEM). Post-explant electrochemistry revealed an impedance curve very different from the pre-implant curve at all frequencies (Figure 2C), whereas the shape and high-frequency impedance remained largely unchanged in the functional array (Figure 2B).

In a logarithmic heat map of bandpower data (Figure 3), the contributing components of the LFP trends are emphasized. The majority of the LFP bandpower was contributed by signals in the delta (0-4 Hz) and theta (4-8 Hz) ranges, with minimal activity or changes happening above 30 Hz.

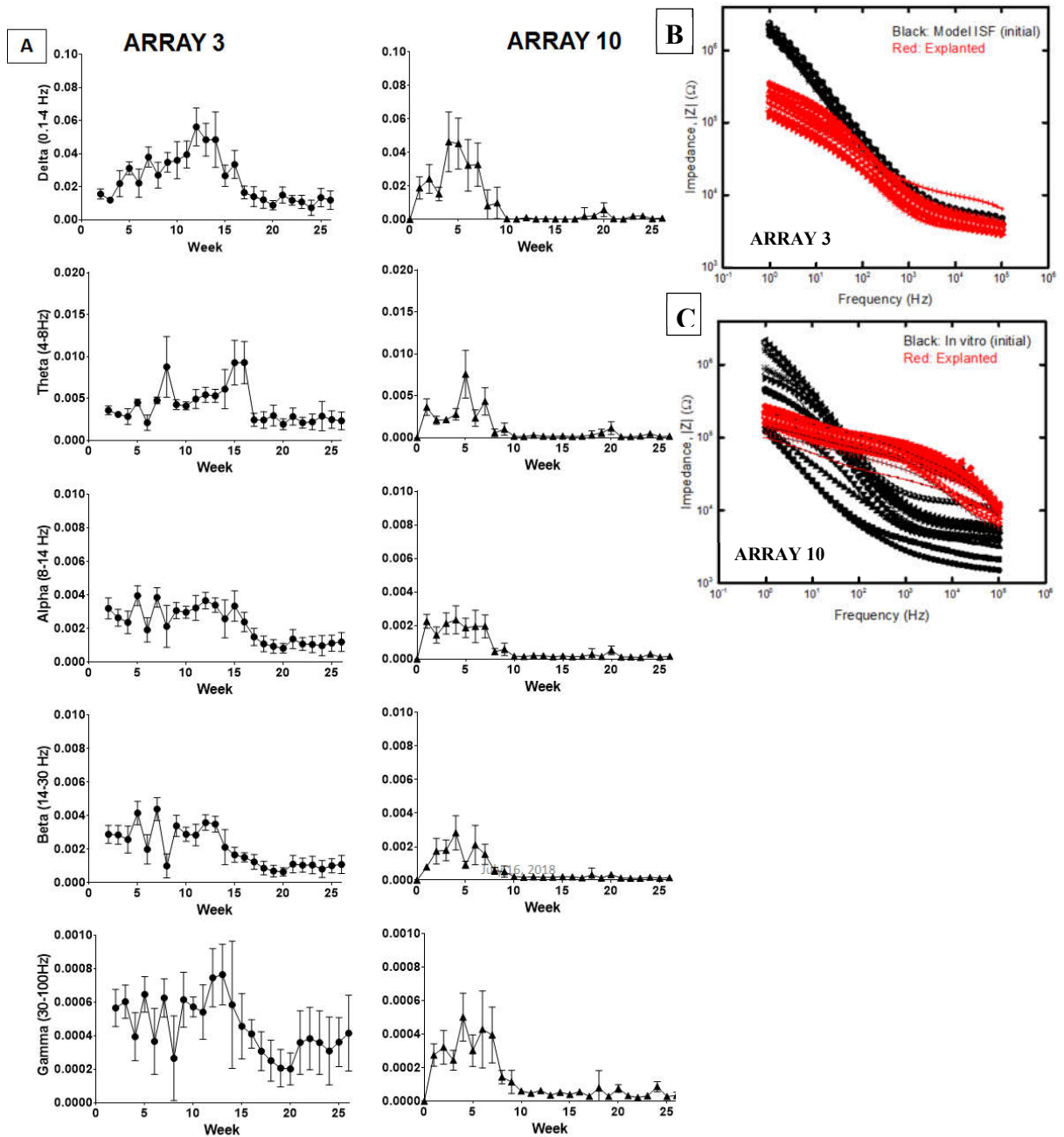


Figure 2: Representative LFP band power to Week 26. Array 3 remained functional until the end of the study, while Array 10 stopped reporting single units from Week 10 onwards. (A) Band power in delta (0-4 Hz), theta (4-8 Hz), alpha (8-14 Hz), beta (14-30 Hz) and gamma (30-100 Hz) bands. (B) EIS of Array 3 shows minimal change pre- and post-implant. (C) EIS of Array 10 is greatly changed between pre- and post-implant in vitro measurements.

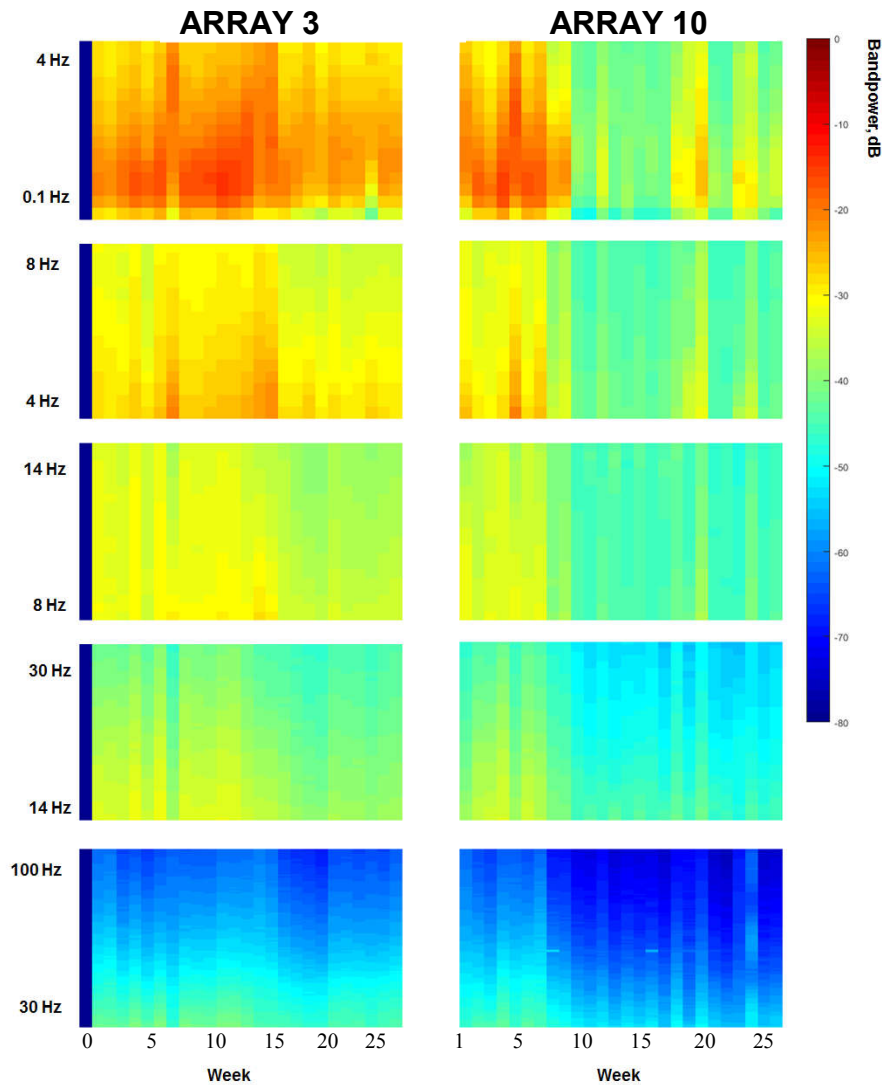


Figure 3: Heat map of bandpower shows changes from week to week on a logarithmic scale. Spontaneous activity is primarily in the 0-8 Hz range, with weaker changes visible between 8-100Hz.

Of the 10 animals in the study, we identified four (Arrays 1,3,6,7) that reliably reported single units until Week 26. Averaging bandpower from 0-100 Hz and other electrochemical measures across all electrodes and animals in this cohort. Outliers beyond two standard deviations from the mean were removed from the dataset. LFP bandpower trend correlated strongly to RMS voltage across the weeks ( $R = 0.96$ ,  $P < 0.001$ ), confirming the belief that LFPs were the primary



component of the wide band recording (Figure 4A). The correlation with total number of single units recorded was much weaker ( $R = 0.67$ ,  $P < 0.001$ ), but still notable. Both measures show a clear decline between weeks 16 and 17, after which the values approach a horizontal asymptote.

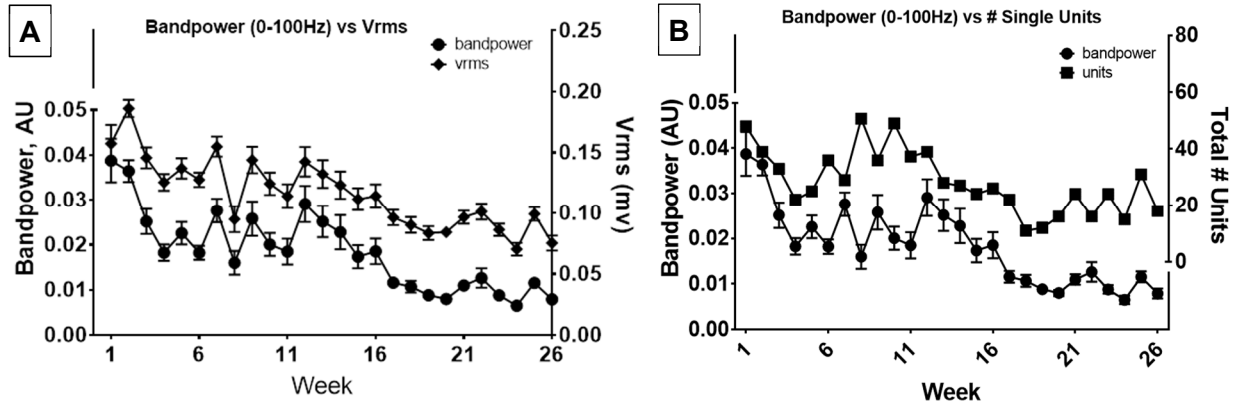


Figure 4: Bandpower vs RMS potential (A) and total # of single units (B). Strong correlation between bandpower and both measures ( $R = 0.95$ ,  $0.67$  respectively). Measures decline gradually, reaching a stable low level around weeks 16-17.

Impedance trends at 1 kHz were largely indifferent to the decline in bandpower ( $R = 0.22$ , Figure 5A). Comparisons at 1 Hz and 100 Hz yielded similar results ( $R = 0.36$ ,  $R = 0.03$ , Figure 5B,C). Other electrochemical measures (charge storage capacity, etc) were equally unremarkable.

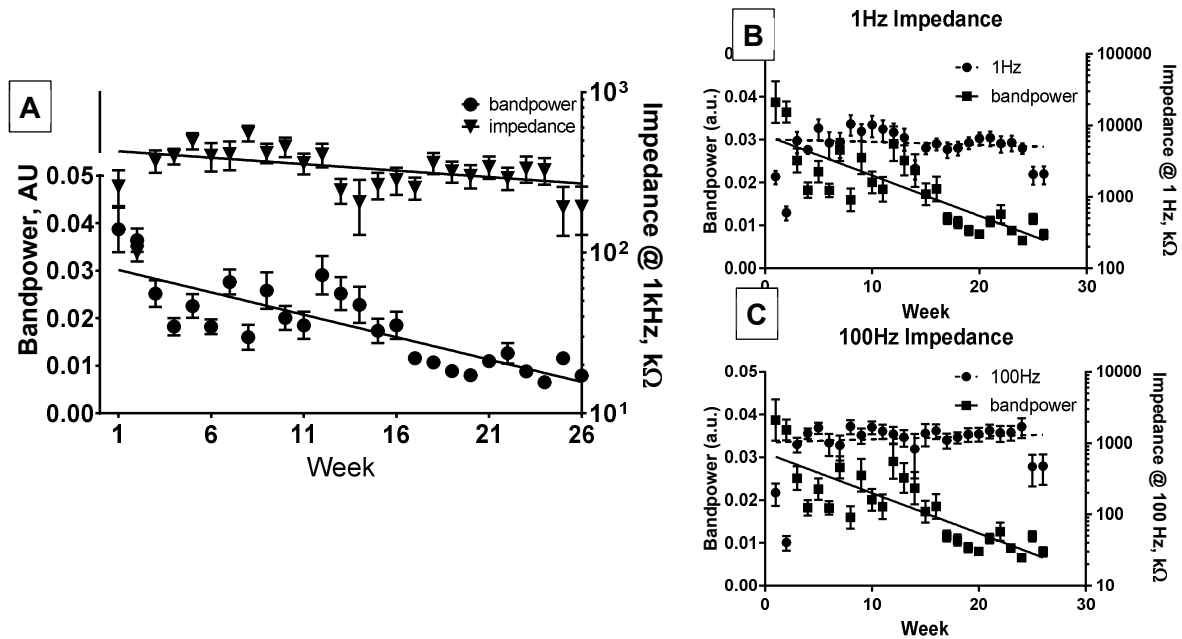


Figure 5: LFP bandpower decline is not correlated with impedance at 1kHz (A), 1Hz (B) or 100Hz (C).  $R = 0.22, 0.36, 0.03$  from A-C.

## 2.4 Discussion

### 2.4.1 Bandpower Trends

We categorized 8 of the 10 animals in the study into one of two categories based on the consistency of single units, LFP bandpower relative to baseline, and a drastic change in pre-implant vs post-explant impedance spectra. The first group was classified as the “Working” group, reporting single units until near the study endpoint and a bandpower significantly different from the saline noise (Arrays 1,3,6,7). The second, or “Non-Working” group reported a sudden drop in single units early (<10 weeks) in the study and thereafter none, as well as saline-level bandpower (Arrays 4, 8, 9, 10). All members of the second group had a visible wire bundle breakage or a dramatic change in impedance spectra consistent with wire breakage. The linear fit to the cumulative bandpower of each group (Figure 6) was not significantly different despite the sudden

drop in bandpower in the second group. This suggests the overall gradual decline in performance is not related to the sudden drop due to wire breakage, but rather some gradual change, the cause of which is yet to be conclusively identified.

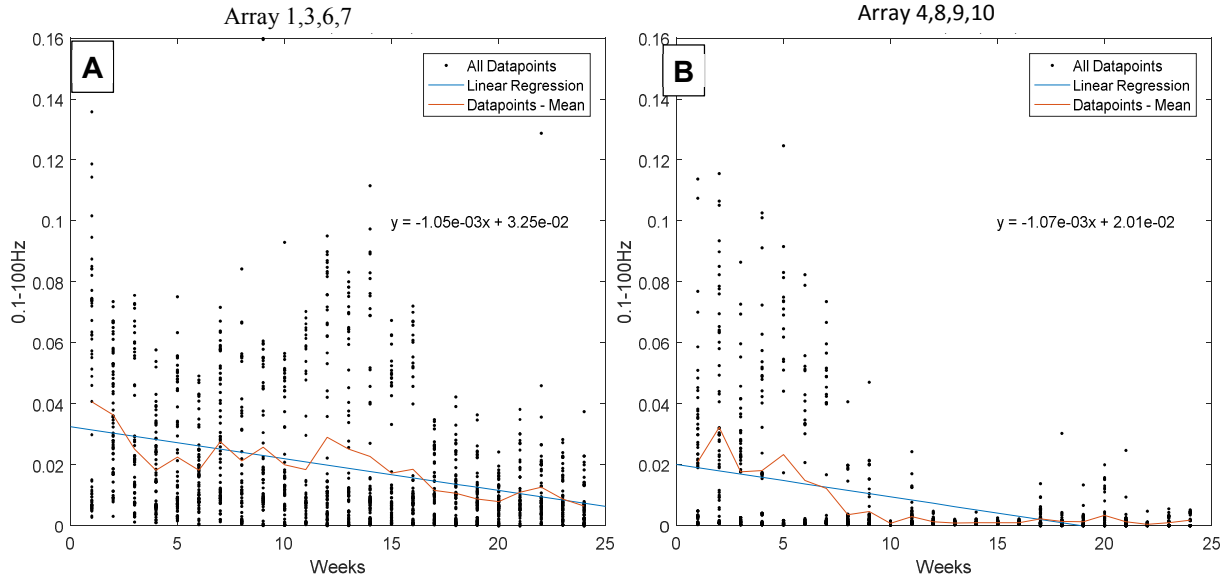


Figure 6: Bandpower in Working vs Non-Working arrays. Linear fit slopes were not significantly different, suggesting there is some cause of gradual decline in performance unrelated to wire bundle breakage reported in Non-Working arrays.

#### 2.4.2 The Relationship between Single-Unit Activity and Local Field Potentials

Although LFPs and spike recordings are extracted from different frequency bands, there exists a poorly defined overlap between the two signals. Both have been successfully used to drive BCI controls, so should be capable of encoding [32], [103], [104]. Alternatively, spike data contaminates LFPs by some unknown mechanism [91]. We observe that multiunit spike bursts coincide with large amplitude LFPs with regularity (Figure 7), even when single units may not be identified.

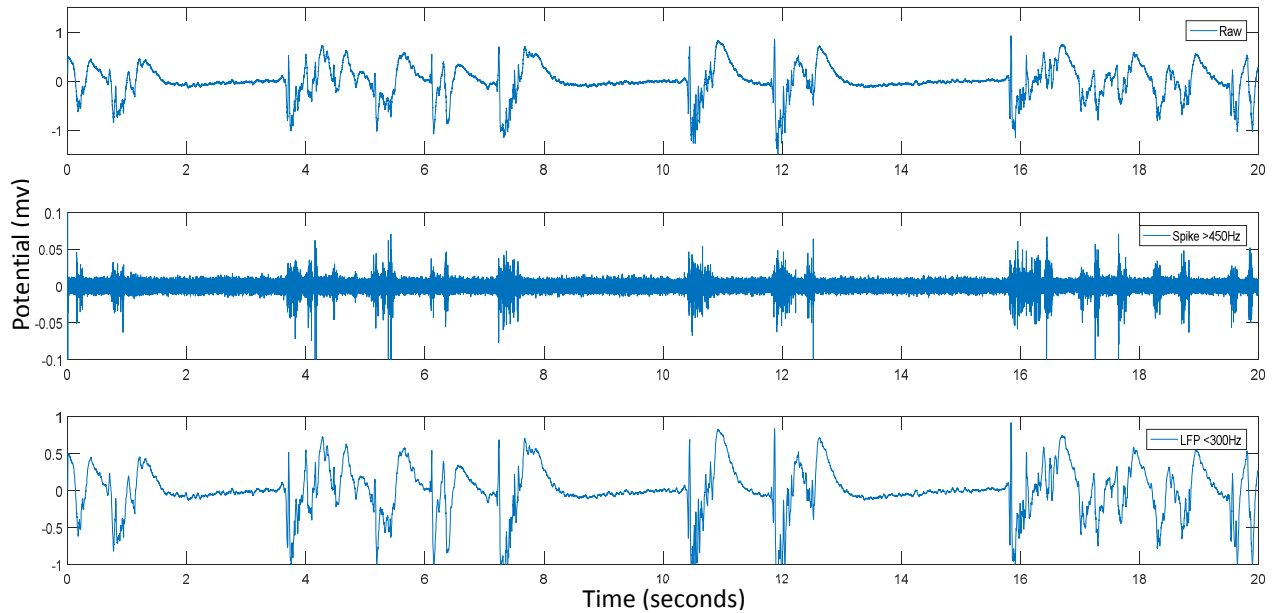


Figure 7: Relationship between Spike and LFP signals. Representative segment from Array 3, Week 12. Spike bursts coincide with large-amplitude LFPs.

We attempted to apply the Working/Non-working discrimination to individual electrodes, but found limited success. There was a weak association between single units and bandpower on a single electrode basis (Figure 8). Low bandpower on a single electrode often coincided with a lack of single units, but not always. Inversely, high bandpower did not guarantee the presence of single units.

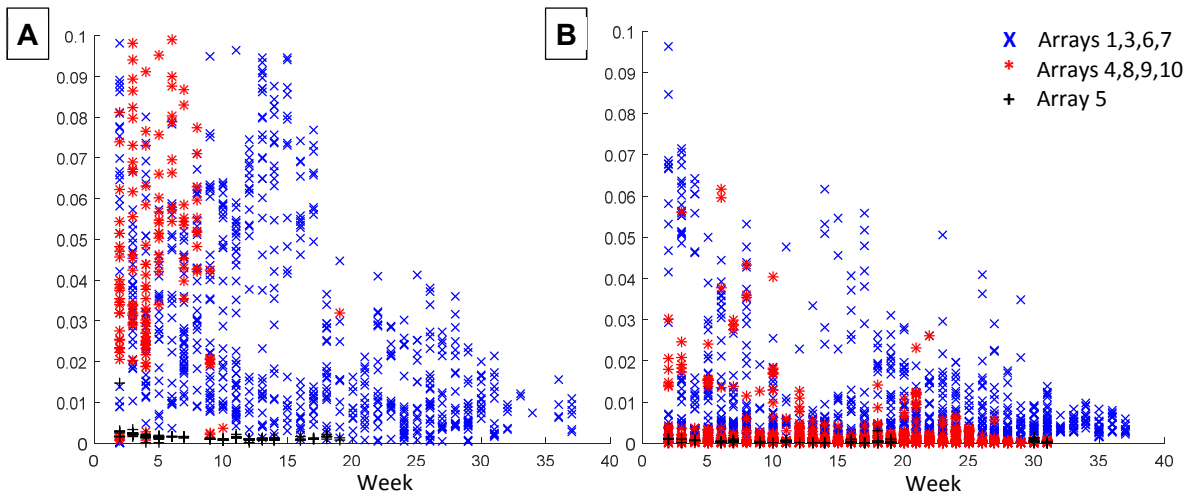


Figure 8: Bandpower over time, in the presence (A) or absence (B) of a single unit recorded on the channel. Points in blue (X-1,3,6,7) came from animals not exhibiting wire breakage. Points in red (\*-4,8,9,10) came from arrays with wire breakage. Array 5 (+) showed wire breakage by Week 19 but reported very low bandpower.

One array could not be categorized, exhibiting a persistently low, saline-level LFP bandpower, but reported single units up until Week 19 (Figure 9). Later, post-explant in vitro EIS suggested wire breakage, but no explanation was found for the low bandpower early in the study.

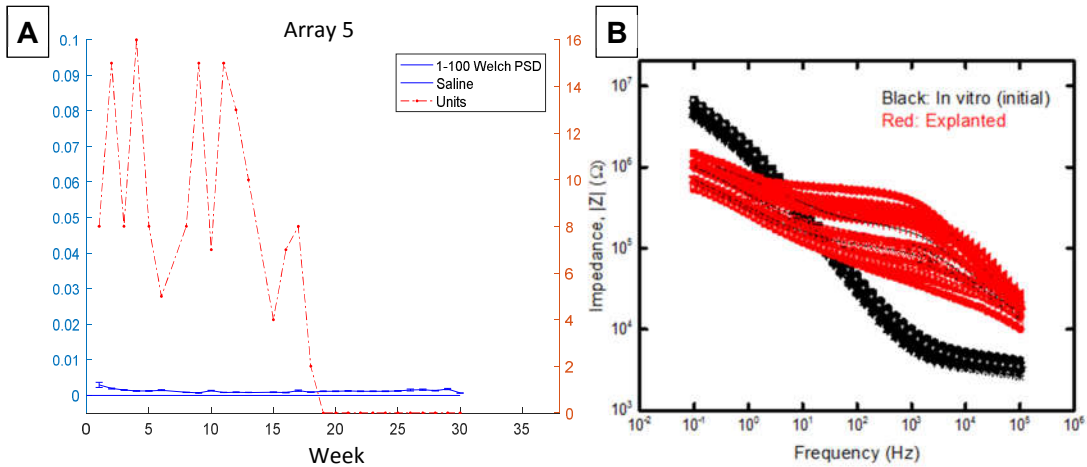


Figure 9: Array 5. (A) An exception to either rule, LFP bandpower was persistently low regardless of the presence or absence of identified single units. (B) Large change between initial and explanted impedance spectra is characteristic of wire bundle breakage.

### 2.4.3 Electrochemistry

We found negligible correlation between impedance and bandpower, reinforcing the biological nature of the decline in bandpower performance. If impedance had significance, we could expect shifts in the frequency spectra as the recording capabilities of the electrode changed—in the absence of such shifts, we can assume that the changes to bandpower are more closely related to the source of the signal than the measurement device.

In this study we report on the chronic behavior of LFPs as recorded under anesthesia by UEAs implanted in rat motor cortex. Within a single session, there exists a strong association between multiunit spike activity filtered from the wide band neural recording and filtered LFPs. LFP bandpower exhibits similar long-term behavior to single unit counts, but are more reflective of the overall magnitude of the signal recorded than the number of single units identified from week to week.

## CHAPTER 3

# A HISTOLOGICAL COMPARISON OF CHRONICALLY IMPLANTED AMORPHOUS SILICON CARBIDE AND PARYLENE-C-COATED UTAH ELECTRODE ARRAYS IN RAT CORTEX

Amorphous silicon carbide deposition was performed by Vindhya Danda. Histology and imaging were performed with assistance from Dr. Mario Romero-Ortega, Dr. Aswini Kanneganti, and Dr. Bryan Black. Scanning electron microscopy was performed by Dr. Alexandra Joshi-Imre. All animal procedures and analysis were conducted by the author with assistance from Dr. Kanneganti.

### 3.1 Introduction

While there now exists a sizable body of literature supporting the viability of brain electrodes, by means of deep brain stimulation [105], [106], intracortical devices are orders of magnitude smaller and more sensitive to tissue changes. Many promising arrays encounter loss of neural signals on a chronic timescale, due to a mixture of abiotic and biotic factors.

The present study focused on the Utah electrode array (UEA), which has shown long-term success in limited human trials for brain-computer interface applications. The UEA is composed of a grid of needle-like machined silicon shanks, each tapering to a point of about 25 microns. The array is coated with an insulating encapsulation material and tipped with conductive metal film. It is capable of spatial specificity and detection of small neural signals, but these advantages drive from several important design features that also present limitations on electrode performance. The small surface of microelectrodes limits flow of current for neural stimulation, and electrode polarization is limited by safety considerations [107], [108]. These limitations incentivize the

testing of metal and oxide electrode films with lower impedance and higher charge delivery capacity for stimulation applications. Encapsulation materials serve a dual purpose in MEAs by preserving signal quality and minimizing tissue response to implanted devices. Ideal encapsulants should be highly insulating with a low dielectric constant and be resistant to corrosion. On a more basic level, the physical integrity of the encapsulation reduces leakage currents that may occur because of encapsulation delamination and cracking. Defects in encapsulation are current shunts, reducing the signal-to-noise ratio and decreasing current delivered during electrical stimulation. These abiotic aspects of neural electrode failure are complicated by the foreign body response.

### **3.1.1 Acute and Chronic Foreign Body Response**

The brain's response to implanted neural devices has been the subject of much research. Though the precise mechanisms are not well understood, the biocompatibility of neural devices has been implicated in their performance [49], [59]. The acute and chronic effects on intracortical electrodes of changes in the tissue surrounding the array may lead to reduced functionality.

Immediately following insertion, microscale hemorrhaging occurs due to damage to major or minor vasculature in and around the path of the device. Bleeding releases cytokines and blood-borne macrophages and is accompanied by swelling. The cytokines cause native microglia and astrocytes to migrate to and proliferate at the site of injury, as well as generate other inflammatory molecules such as reactive oxygen species.

Microglia are macrophage-like cells exclusive to the central nervous system. When activated, they condense from branched bodies, not unlike astrocytes, into dense amoeboids, acting as cytotoxic cells and phagocytes and secreting proteolytic enzymes [50]. However, microglia



release both neurotrophic and neurotoxic factors, complicating their role in the foreign body response. Under in vitro conditions, microglia have been found to secrete BDNF and NGF [109], both neuronal growth factors, but when activated by injury in vivo will secrete various reactive oxygen intermediates and neurotoxins, which are thought to damage neurons or implants [110].

Astrocytes are star-shaped glial cells that perform a multitude of supporting functions in the CNS and form a major component of the blood brain barrier. In their reactive state, they grow in size and increase the production of extracellular matrix [50]. Additionally, they increase expression of glial fibrillary acid protein (GFAP), which is exclusive to astrocytes and is a useful marker for discrimination.

The persistent presence of implanted intracortical electrodes elicits a chronic response after the decline of the acute response. Electrodes are too large to allow for phagocytosis; instead, activated microglia and astrocytes weave together with fibroblasts to form a sheath commonly referred to as a glial scar [111]. Microglia will also fuse into larger, multi-nucleated cells similar to fused macrophages seen in chronic inflammation elsewhere in the body [112]. In addition to glial cell aggregation, connective tissue such as meningeal fibroblasts are often discovered in and around cortical implants [34], eventually physically dislodging the implant [51]. Neuronal density changes in the proximity of the electrode is another postulated cause of the decline in chronic signal performance, either by displacement by glial cells or neurotoxic effects. Reports of the radius of this effect range from 1  $\mu\text{m}$ , or non-existent, to over 100  $\mu\text{m}$  [50]. Presumably, the lack of neurons within the electrical recording range of the electrode would lead to an absence of detectable activity. In addition, neuronal death caused by neurotoxic factors will lead to loss of signal, as will excessive glial encapsulation, which creates a resistive barrier surrounding the

electrode. These changes have been observed consistently in multiple experiments in conjunction with a decline in electrode performance, but a direct causal link has yet to be established.

### **3.1.2 Amorphous Silicon Carbide**

As a thin film, amorphous silicon carbide (a-SiC) has found use in a number of biomedical applications, both as a substrate and coating. It is chemically inert and resistant to dissolution [113], and is less prone to platelet and fibrin activation when used as a stent coating [114]. It may be deposited in conditions compatible with many other polymers, and is resistant to high temperatures. Electrically, a-SiC has a high dielectric constant and resistivity. Work establishing the suitability of a-SiC [56], [58], [113], [115] for intracortical implants suggests a-SiC would be good alternative to conventional Parylene-C based coatings for the UEA.

Understanding the biological response to a material is valuable in untangling the biotic factors associated with intracortical device failure. The aim of this study was to provide a direct comparison of the tissue response of a-SiC against the more conventional Parylene-C on an established neural device, the UEA. Other authors have compared the performance of a-SiC against bare silicon on a Michigan probe [58] for up to 8 weeks, Parylene C against bare silicon [60] on a single shank array up to 12 weeks, and Parylene C for up to 12 weeks on the UEA [59]. We used immunohistochemical labelling of neurons, astrocytes, and activated microglia at 60, 90, and 120 days to assess the chronic tissue response.

## 3.2 Methods

### 3.2.1 Utah Electrode Array

Utah-style microelectrode arrays (UEAs), coated with Parylene-C and uncoated, were purchased from Blackrock Microsystems (Salt Lake City, Utah). Arrays had a 4x4 rectangular grid of 1mm long electrodes spaced 400  $\mu\text{m}$  apart.

Bare silicon 10 x 10 UEAs were coated with a-SiC using plasma enhanced chemical vapor deposition before being cut to 4x4 arrays. The backside of the arrays were coated with medical grade silicone (NuSil-Avantor MED6-6606) and allowed to cure (Figure 10). Arrays were non-functional and untethered. Tips were not etched or coated with metal.

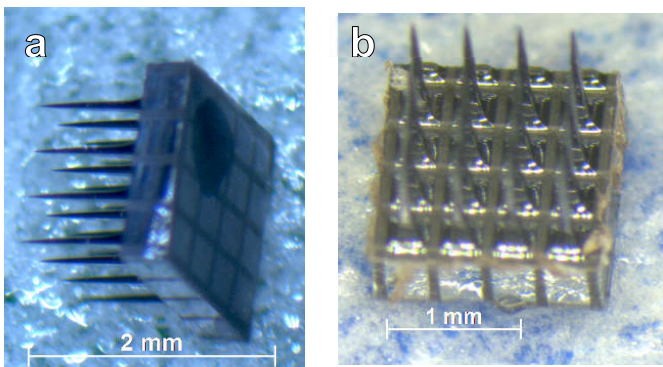


Figure 10: UEA with silicone backside encapsulation. Mark on backside (a) to indicate array orientation. (b) 4x4 grid of electrode shanks with 400  $\mu\text{m}$  pitch and 1 mm length.

### 3.2.2 Animal Procedures

All procedures involving animals were approved by the University of Texas at Dallas Animal Care and Use Committee. Adult male Long-Evans rats weighing between 300-350g (N = 27, Table 1) were anesthetized with ketamine (65mg/kg) xylazine (13.33mg/kg) acepromazine (1.5mg/kg) mixture administered intraperitoneally, in conjunction with atropine sulfate (0.05mg/kg) administered intramuscularly. The plane of anesthesia was maintained as needed with

isoflurane. The animals were placed in a stereotaxic frame and disinfected on the scalp with 70% isopropyl wipes and betadine. Lidocaine was administered as a local anesthetic around the stereotaxic bars. Dexamethasone (2mg/kg) was administered subcutaneously to reduce cerebral edema. The skull was exposed with a midline incision, and the scalp and fascia retracted. Holes for anchor screws were drilled with a stereotaxic fixed drill at least 1.5 mm lateral, 2.0 mm anterior and 2.0mm lateral, 6.0 mm posterior relative to cranial sutures (Figure 11).

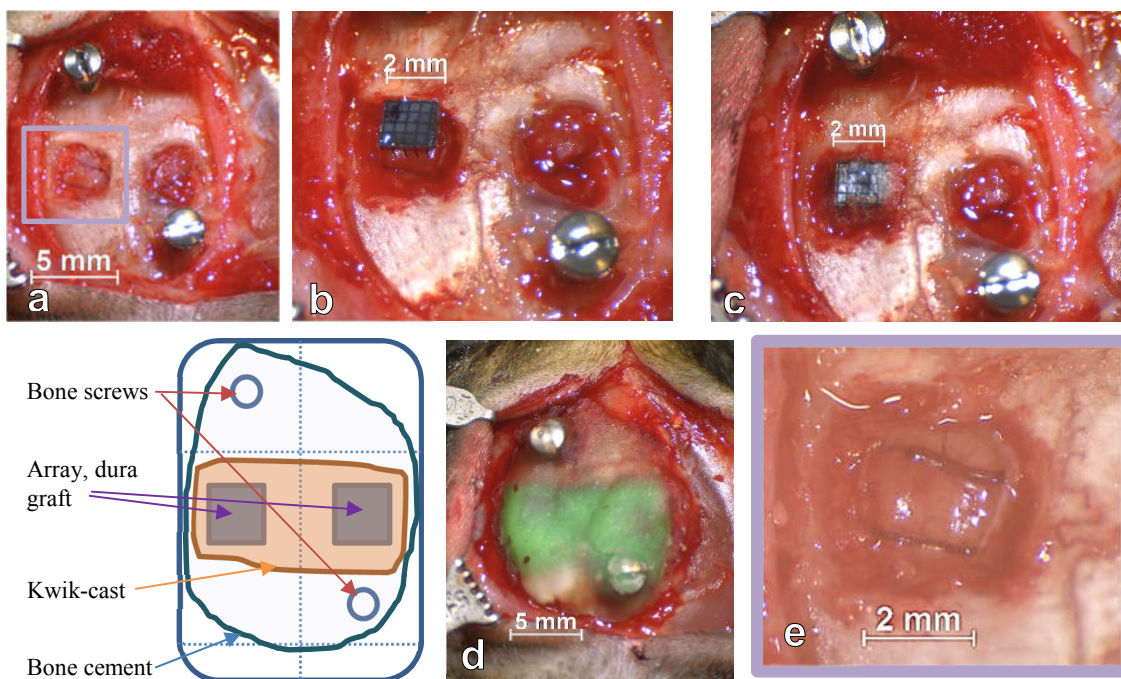


Figure 11: Bilateral craniotomy and implant of UEA. (a) Placement of craniotomy and screws relative to cranial sutures. (b) Untethered UEA resting on brain prior to insertion. (c) Bilateral insertion of UEAs, covered with collagen-based dura graft. (d) Craniotomy sealed with medical-grade silicone and bone cement anchored to screws. (e) Blood vessels at implant site, typically present.

Two craniotomies approximately 2.5 mm x 2.5mm were created over the left and right somatosensory cortices (Figure 11), beginning 1.5mm from the bregma using a hand drill and sterile saline rinses to prevent overheating. A 30 gauge needle, #5 forceps, and spring scissors were used to pierce and reflect the dura.

The array was placed on the surface of the brain before being inserted with a pneumatic inserter (Blackrock Microsystems) at 1m/s. The array was covered with a collagen-based dural graft (Biodesign Dural Graft, Cook Medical, USA) followed by silicone elastomer (Kwik-Cast, WPI), and bone cement (Stoelting Co, IL). Suture clips were used to close the incision above the head cap. Buprenorphine SR (0.15mg/kg) and cefazolin (5mg/kg) were administered to manage post-operative pain and infection, respectively. Animals from each group were sacrificed at 60, 90, and 120 days, for a total of 6 implanted arrays in 3 animals per material per time point.

Table 1: Experimental Groups. Animals were bilaterally implanted with arrays in the somatosensory cortex. A total of 54 devices (n=6) was implanted in 27 animals.

Animals per group	Amorphous Silicon Carbide	ParyleneC	Silicon, bare
60 days	3 (6 devices)	3 (6 devices)	3 (6 devices)
90 days	3 (6 devices)	3 (6 devices)	3 (6 devices)
120 days	3 (6 devices)	3 (6 devices)	3 (6 devices)

At sacrifice, animals were anesthetized with sodium pentobarbital and transcardially perfused with 0.9% saline, followed by 4% paraformaldehyde in PBS. Brains and arrays were extracted from the skull. Brains were post-fixed for an additional 24 hours in 4% paraformaldehyde and embedded in 6% agarose for improved rigidity and to preserve irregular tissue structures. Horizontal brain sections 150  $\mu$ m thick were taken using a vibratome.

### 3.2.3 Immunohistochemistry

Immunohistochemical analysis (IHC) was performed on a single slice at a depth of approximately 300-450  $\mu$ m roughly parallel to the plane of the array. Free-floating brain sections were washed with PBS and quenched with 0.16M NaBH<sub>4</sub> for 30 minutes to reduce auto fluorescence. Slices were blocked for 4 hours in PBS with 4% v/v goat serum (Gibco, Carlsbad,

CA) and 0.3% v/v Triton-X 100, then incubated overnight at 4°C in PBS with 4% v/v goat serum (Gibco, Carlsbad, CA) and 0.1% v/v Triton-X 100 and the following primary antibodies: NeuN (EMD Millipore, Canada, 1:500), GFAP (EMD Millipore, Canada, 1:500), and CD68 (Ab-3, Thermo Scientific, 1:250). Fluorescent secondary antibodies (Alexa 405, 488, 532; 1:1000) were incubated at room temperature for 2 hours. All incubations were performed on an orbital shaker with 4 washes in PBS between steps. Sections were washed for a final time and mounted and coverslipped in Fluoromount-G (Southern Biotech), then imaged with a confocal microscope using a 20X objective (Nikon). Each array region was imaged using stitching and Z-stacks to produce a maximum intensity projection.

### **3.2.4 Image Quantification**

To quantify images for comparison, we calculated the relative intensity of staining as a function of the distance from the electrode using a custom MATLAB (Mathworks, MA) script (Figure 12) employing methods reported by Goss-Varley et al., [116]. In summary, electrode holes were defined manually, then dilated into a set of concentric rings in 5  $\mu\text{m}$  steps. In each ring, the total fluorescent intensity of the marker was summed and normalized to the area of the ring. Defects in the tissue were excluded from the tissue in manually defined regions. Neurons were counted manually in bands of 50  $\mu\text{m}$ . Intensity per unit area was normalized to a control slide stained with no primary antibody.

Comparisons between material (Parylene-C, a-SiC, Si), time (60, 90, 120 days), and distance (0-250 $\mu\text{m}$ ) used a three-way mixed ANOVA, using Material and Time as between-subjects factors and Distance within-subjects, and multiple comparisons test in MATLAB.

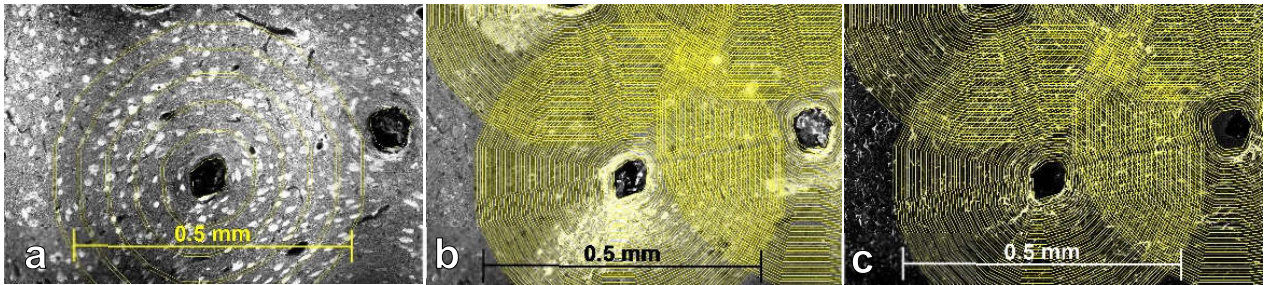


Figure 12: Custom program for image quantification. Composite images for each array were imported into MATLAB, and electrode locations were manually defined. Concentric bands were defined from each electrode. Intensity of CD68 and GFAP expression were calculated automatically in 5  $\mu\text{m}$  bands, while neurons were manually counted in 25  $\mu\text{m}$  bands, to a maximum of 250  $\mu\text{m}$  from the electrode. (a) NeuN. (b) CD68. (c) GFAP.

### 3.3 Results

All but two animals survived until the cohort endpoint, dying from complications within a week of surgery. One died of adverse reaction to analgesia 1 day postoperative. The other died 4 days post-operative. Explant revealed a large subcutaneous clot at the surgical site above the bone cement enclosing the craniotomy, and blood on the surface of the brain (Figure 13). Bleeding was most likely caused by the device, but would needed to have occurred post-operatively. The device was removed post mortem and cleaned before being implanted in another animal, and did not result in dramatically different results.

For all but three of 54 arrays, removal post-fixation did not cause tearing of brain tissue. Arrays were covered with a mixture of fibrous tissue and cellular debris (Figure 14). This material was not always visible unaided.

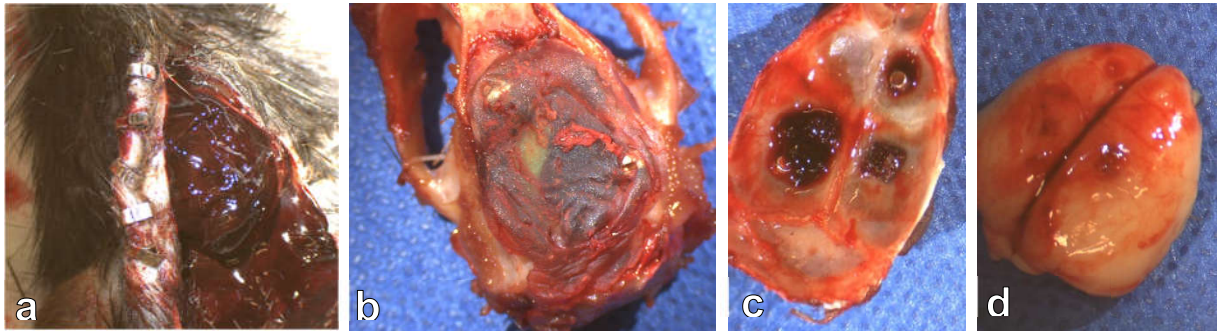


Figure 13: Cranial bleeding caused premature death. Array geometry causes significant vascular damage in rat. (a) Subcutaneous hematoma. (b) Bleeding evident beneath bone cement around right craniotomy. (c,d) Remnants of severe bleeding seen from inside the skull.

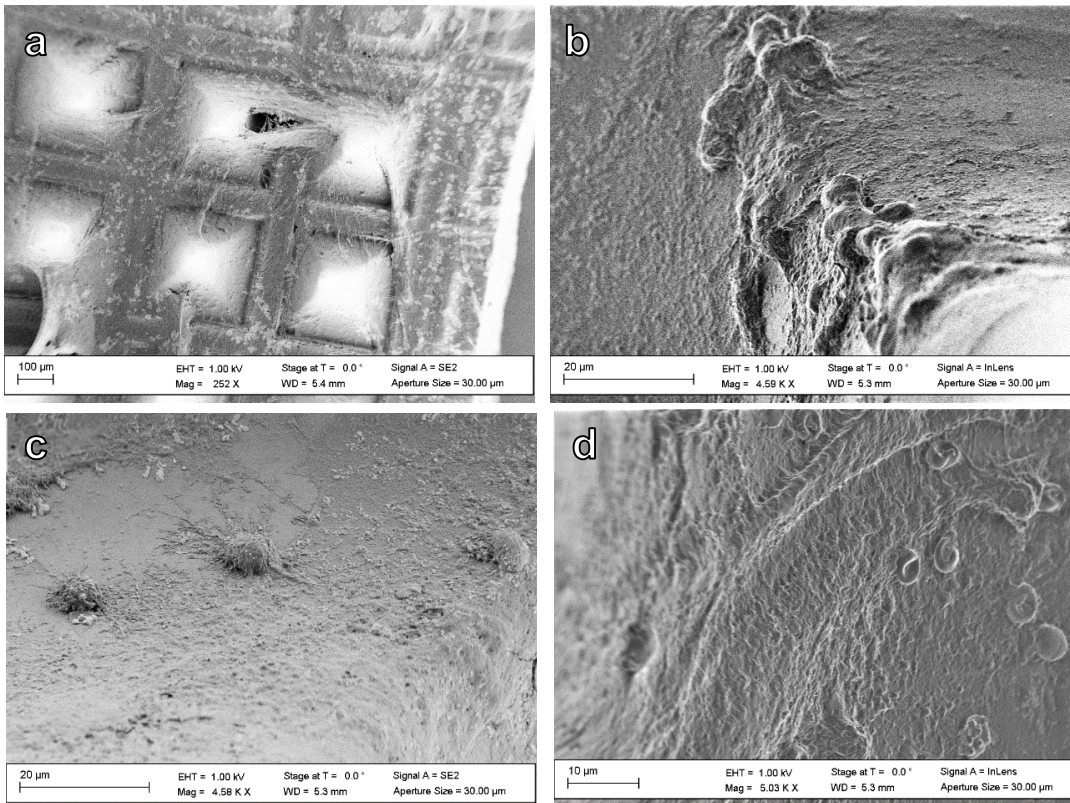


Figure 14: SEM images of arrays showing fibrous and cellular adherents following explant. (a,b,c) Unspecified cell adherents on the surface of the array. (d) RBCs.

Tissue adhesion to the array ranged from nonexistent (Figure 15a) to mild (Figure 15b, c) or severe (Figure 15d). We observed many explants to have a filmy layer of collagenous tissue (Figure 15c) that was contiguous with the dura between the shanks of the array. This tissue did not



appear to adhere to the surface of the brain but was coincidental with mild (Figure 15f) and severe lesion formation (Figure 15e). However, lesion severity was not always associated with equivalent tissue adhesion. Severely discolored residue on the explanted array (Figure 15b) or tissue (Figure 15f, h) was consistent with surgical records of intraoperative bleeding immediately preceding or following array implantation.

We also observed significant vertical tissue displacement (Figure 15h,i) surrounding the implant in the craniotomy opening, creating a crown of tissue around the edges that held the device in the tissue during explant. On the surface of the brain, there was visible patterning from the grooves of glass filler at the base of the electrode shanks.

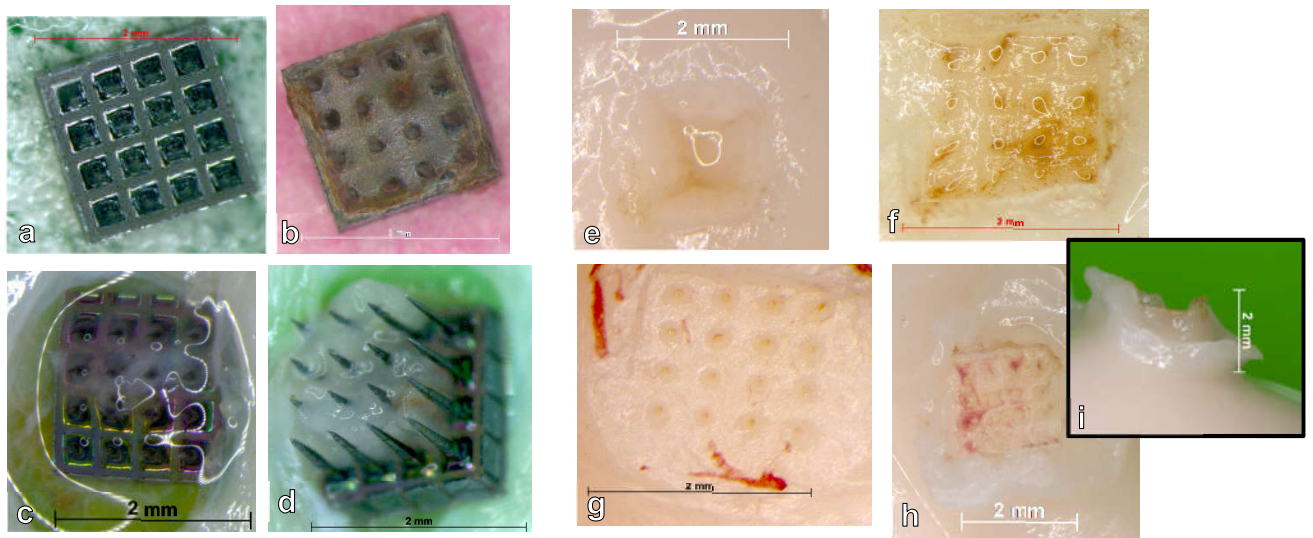


Figure 15: UEA explant. Optical photographs showing typical (a-c, e-g) and atypical (d,h,i) array and tissue condition. Residue from bleeding can be seen in on both the array (b) and tissue (f,g,h). Lesion severity ranged from mild (f) to severe (e), eliminating any trace of individual electrode shanks.

Table 2: Gross histology overview, based on typical outcomes described in Figure 15. There was no correlation between encapsulation or implant duration and outcomes. ASC = amorphous silicon carbide. BSI = bare silicon. PLC = Parylene-C.

By	Good markings (g)	Markings + Displacement (h)	Dimple (e)	Dimple + electrodes (f)	tissue tear (d)	array residue (b)
	20	10	8	13	3	10
By Cohort						
ASC, 60	2	0	1	2	1	3
BSI, 60	1	3	1	1	0	1
PLC, 60	4	1	0	1	0	0
ASC, 90	3	1	0	2	0	0
BSI, 90	1	0	3	2	0	0
PLC, 90	3	2	0	1	0	2
ASC, 120	1	1	2	1	1	1
BSI, 120	4	2	0	0	0	2
PLC, 120	1	0	1	3	1	1
By Encapsulation						
ASC	6	2	3	5	2	4
BSI	6	5	4	3	0	3
PLC	8	3	1	5	1	3
By Time Point						
60 days	7	4	2	4	1	4
90 days	7	3	3	5	0	2
120 days	6	3	3	4	2	4

### 3.3.2 Immunohistochemical Analysis

IHC labelling was used to quantify the presence of neurons (NeuN), reactive astrocytes (GFAP), and activated microglia (CD68) as a function of distance from the edge of electrode perforations. Control samples treated with the absence of primary antibodies showed minimal non-specific binding (Figure 16).

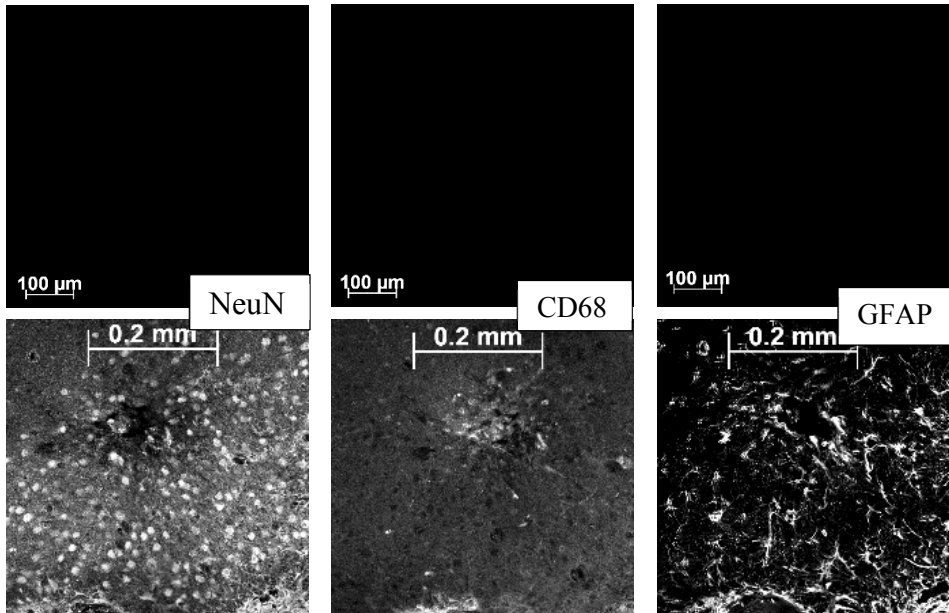


Figure 16: Representative images as compared to no primary antibody controls. Controls showed minimal nonspecific binding and served as a value for normalization.

### Neuronal Density

NeuN labeling showed an increase in neurons up to 100  $\mu\text{m}$  from the electrode edge, with a slight decline beyond 200  $\mu\text{m}$  as the tissue fell into the radius of adjacent electrodes (Figure 17). This trend was present at all time points and materials, but weaker at 90 days for bare silicon and a-SiC, and 120 days for a-SiC. Two-way ANOVA comparisons of material with distance and multiple comparisons tests showed a significant difference in adverse immune response between ParyleneC and a-SiC at all time points ( $P < 0.0001$ ).

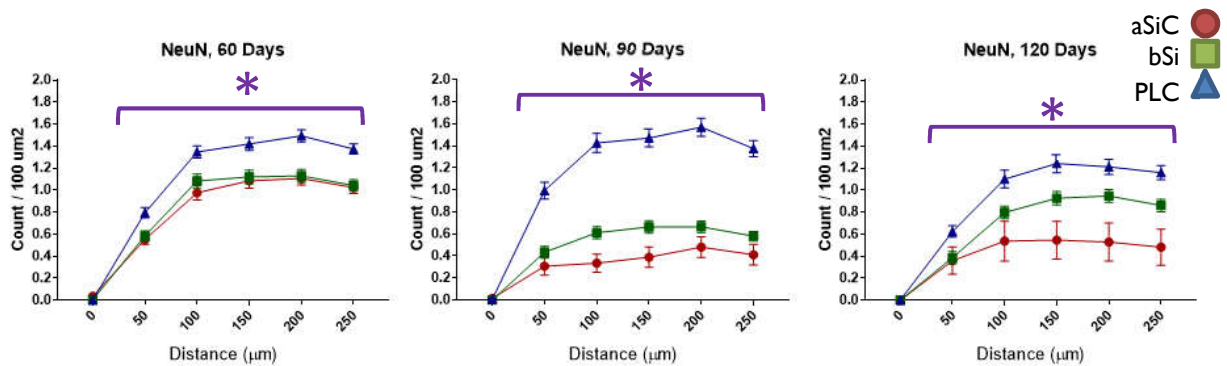


Figure 17: Normalized neuronal density per unit area  $\pm$  SEM as a function of distance from the edge of the electrode across all shanks in arrays. \*Parylene-C density is significantly higher ( $P < 0.0001$ ) than a-SiC at all distances and time points.

### Astrocyte Activation

Inversely to what we observed with NeuN, GFAP expression was highest adjacent to the electrode location and declined with distance (Figure 18). Up to 30  $\mu\text{m}$  from the electrode edge there was an increased level of activated astrocytes, after which it generally remained steady. A-SiC generated a stronger activation of astrocytes than Parylene-C at 60 and 120 days, but at 90 days the difference was only significant between 70 and 205  $\mu\text{m}$  from the electrode site ( $P < 0.0001$ ).

### Microglia Activation

CD68 labelling revealed a similar response in the increased presence of activated microglia and macrophages in close proximity to the electrode, up to 30  $\mu\text{m}$  from the electrode edge (Figure 19). Microglia presence was significantly less in Parylene-C than a-SiC up to 25  $\mu\text{m}$  from the electrode. At 60 days there was no significant difference beyond 120  $\mu\text{m}$ , but at 90 and 120 days there was none beyond only 30  $\mu\text{m}$  ( $P < 0.0001$ ).

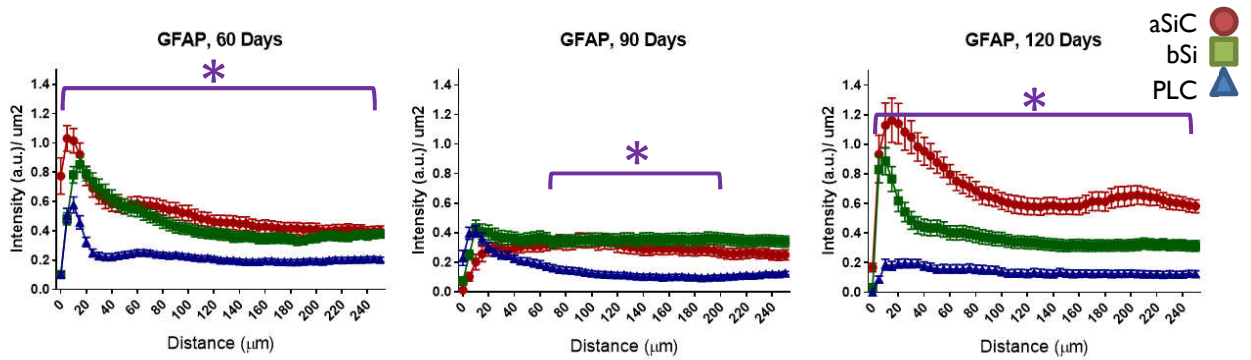


Figure 18: Normalized GFAP fluorescence intensity  $\pm$  SEM as a function of distance from electrode hole edge. There was a noticeable difference in response within a radius of 30  $\mu\text{m}$ , after which the presence of astrocytes was fairly uniform. Difference between materials was most significant at 60 and 120 days ( $P < 0.0001$ ).

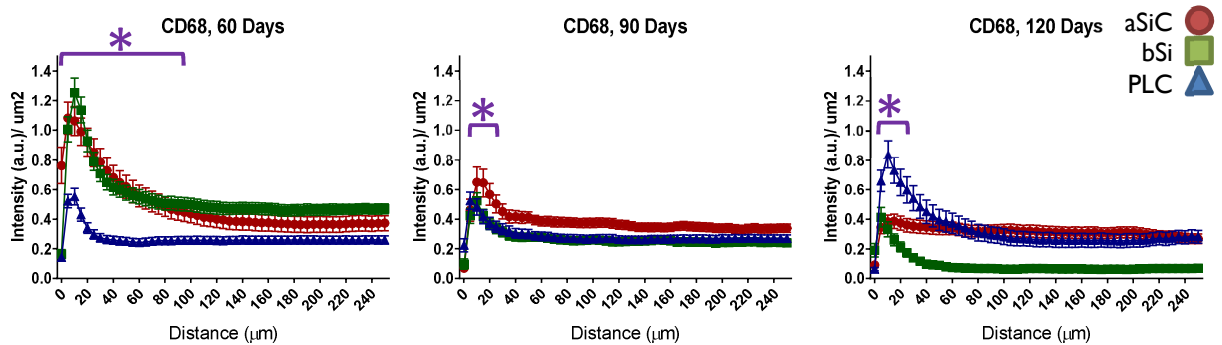


Figure 19: Normalized fluorescence intensity  $\pm$  SEM of CD68 as a function of distance. The difference between Parylene-C and a-SiC was significant within a small radius of the electrode.

### 3.4 Discussion

Using fluorescence based immunohistochemistry, we quantified the neuroinflammatory response of a-SiC, Parylene-C, and uncoated Si UEAs. Our results indicate a-SiC is comparable to control Si devices, but they are generally worse than conventional Parylene-C coated arrays. We found within a limited distance of the electrode, there was typically a heightened response of astrocytes and microglia, in conjunction with the reduced presence of neurons. These results are largely in line with shorter or parallel duration material comparisons of intracortical implants,

using different structures in rabbit [113] or rat [58], [60]. For the most part, there was a significant decrease in all cell types between 60 and 120 days, suggesting there are additional changes taking place in this time frame. Brains implanted with Parylene-C reliably showed increased neuronal density and decreased astrocyte and microglia activity.

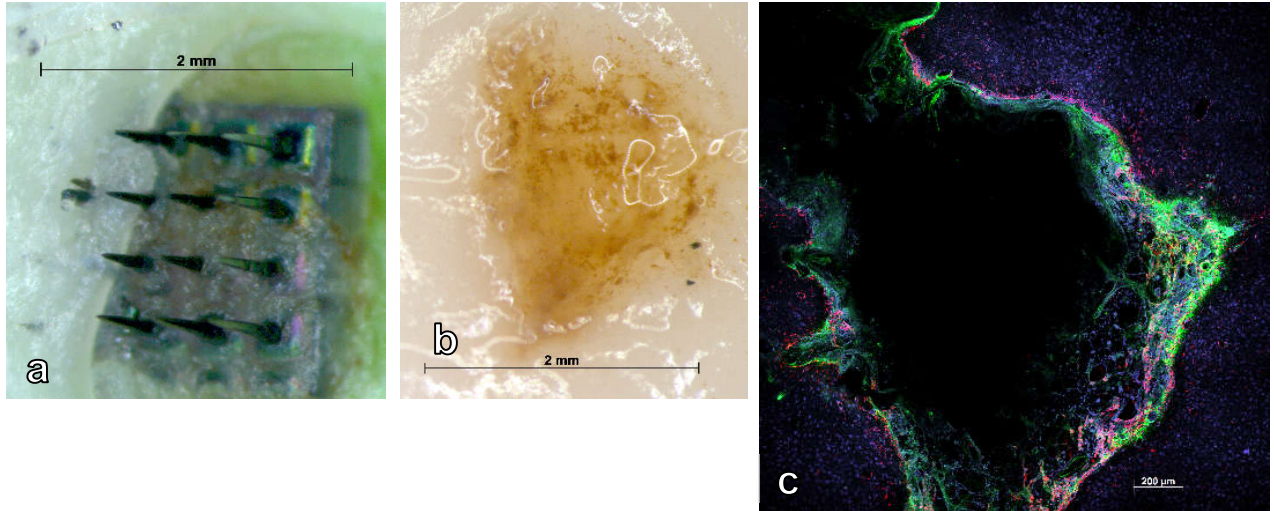


Figure 20: Absence of electrode perforations as a result of lesion. (a) Error in implant placed device at an angle, and collagenous adhesions are visible on the surface of the array. (b) Large lesion and discoloration in the surface of the brain, as well as the absence of clear electrode holes. (c) Edges showed a mixture of CD68 and GFAP expression, but few recognizable cell bodies.

A minimum of three slices ( $n = 6$ ) were analyzed per experimental group, with exceptions made in the case where there were few intact electrodes in the slice due to larger lesion formation (Figure 20). We observed large lesions beneath the surface of the array extending as deep as about 500  $\mu\text{m}$  in 31 of the 54 arrays implanted. The incidence of these lesions was not correlated with encapsulation material or implant duration treatment groups (Table 2). Similar observations have been made with Parylene-C and a-SiC insulated 16-electrode UEAs in chronic electrophysiology and electrochemistry studies at UT Dallas in rat cortex [61]. In addition, Nolte et al. [59] reported the formation of large lesions under 16-shank UEAs implanted in rat cortex, presenting as early

as 4 weeks in stab wounded animals as well as chronic implants. They ascribe the formation of the lesions primarily to vascular injury associated with mechanical damage during insertion. The lesions comprise of macrophages, microglia, and an apparent extracellular matrix material, but no neurons. Our own studies showed similarly high levels of gliosis in cavity regions in conjunction with the absence of neurons. The consequences of the extensive loss of cortical neurons and the persistent glial activity within the lesion on the chronic tissue response to the coated-shanks outside the lesion are unclear. The depth at which we analyzed our tissue (300-450 $\mu$ m) is not close to the recording tip, and thus may have little effect on recording capability. However, the severity and frequency of the lesions do suggest that the UEA is at best only marginally tolerated in rat cortical preparations and that this response is related to insertion trauma and size of the implanted electrodes.

Another concern was the method of taking tissue slices. While the 4x4 UEA is reasonably well tolerated by the rat brain, the local swelling during surgery and curved surface of the brain make a truly planar implantation unrealistic (Figure 21c). Under magnification, inconsistencies in the depth of the tissue slice became evident, by the variation in size of electrodes delineated. Given the effect of electrode size on foreign body response, the variation of hole sizes in these samples weakens the assumption of a fixed depth and size (Figure 21b). In a single slice, the electrodes can differ quite noticeably, from 100  $\mu$ m across to the absence of a clear hole, in which case the position of the electrode tip is extrapolated from existing holes (Figure 21a).

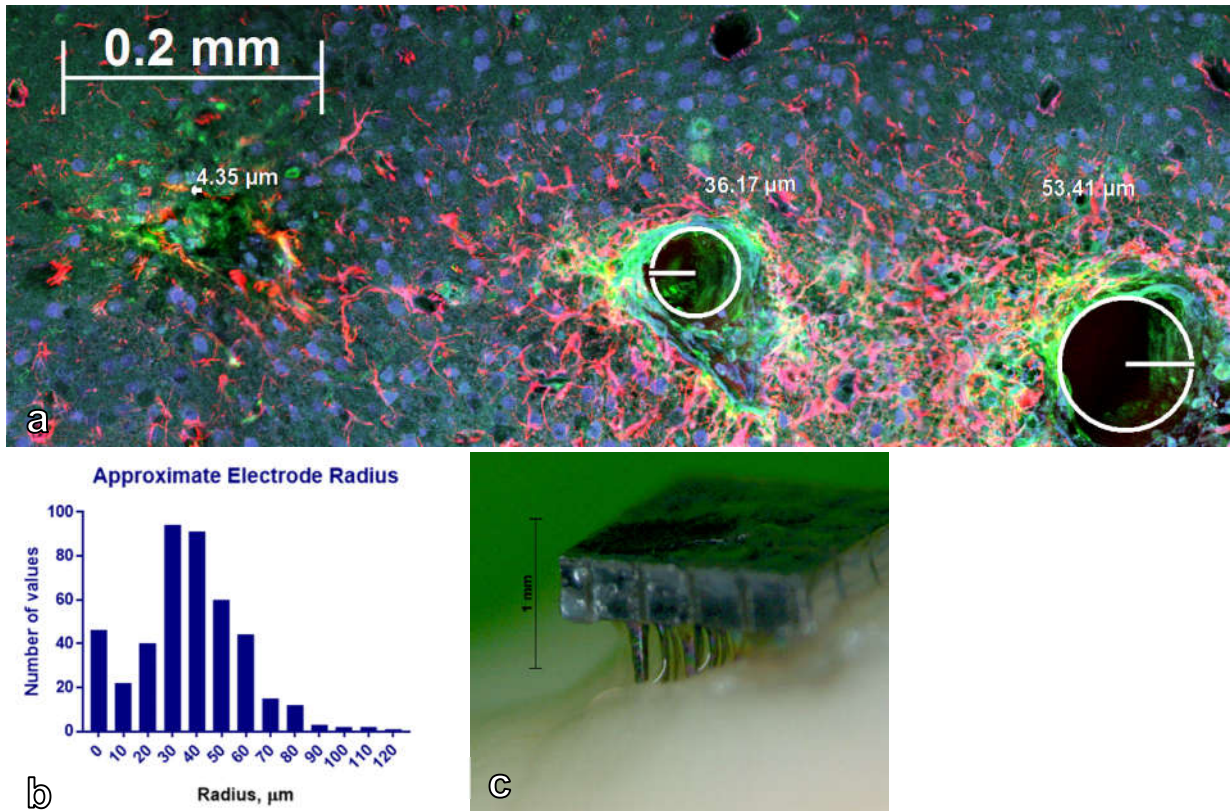


Figure 21: Discrepancies in electrode perforation size at a nominal slice depth. (a) Different size electrode holes in a single slice shows a skewed plane of slicing. (b) Electrode size across all assessed samples with at least 1 definitive electrode hole. Radius 0 indicates the absence of an electrode hole. (c) Explant reveals implant is not certain to be flush to the surface of the brain, and therefore not at a consistent depth.

Control slices showed no auto fluorescence under confocal microscopy in all wavelengths and filters. However, tissue discoloration translated into heavy fluorescence intensity across all channels, casting doubt on the level of nonspecific binding (Figure 22). This discoloration could be observed on the surface of nearly every sample, and extended the full depth of observed lesions.



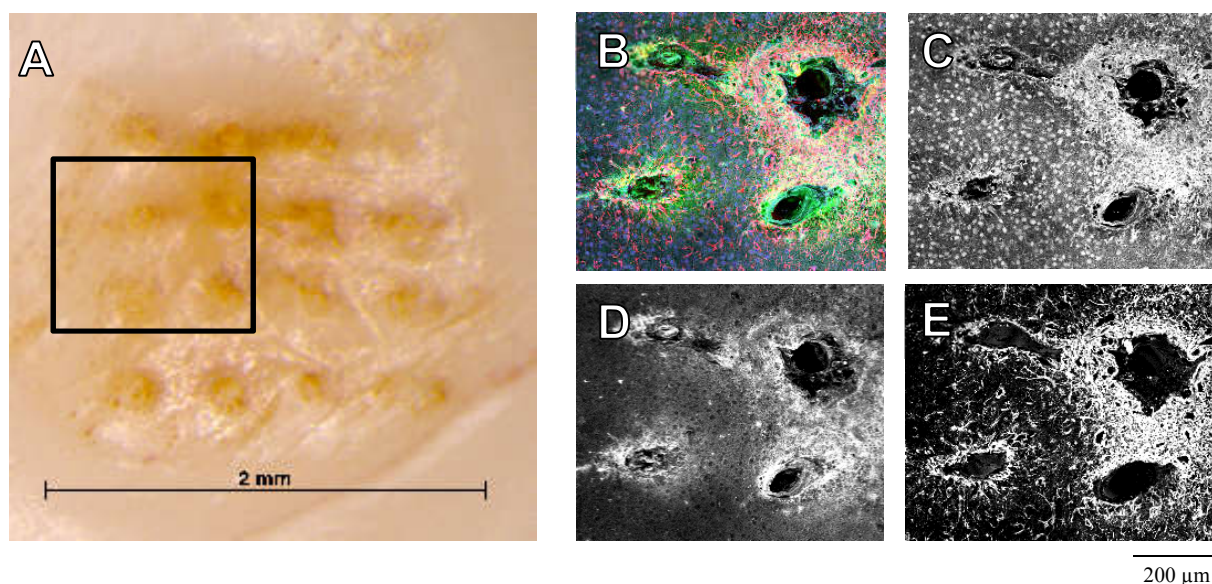


Figure 22: Discoloration of unstained tissue surface (A) corresponds to large areas of fluorescent antibody binding in all channels. (B) shows superimposed fluorescent staining of highlighted region from NeuN (C, blue), CD68 (D, green) and GFAP (E, red).

Within the array there could be a high degree of variability in the fluorescent intensity surrounding tissue, based on the position of the array and as an artifact of the surface lesions (Figure 23). When large lesions were not present, thinner regions dominated by glial tissue, either astrocytes, microglia, or a mixture of such were observed. Neuronal intensity was noticeably different at 90 and 120 days when electrode position was considered. The high variability in CD68 and astrocyte expression is more difficult to interpret. Further research must go into analyzing the tissue closer to the electrode tip, where presumably the effect of surface lesions and electrode site may be lessened.

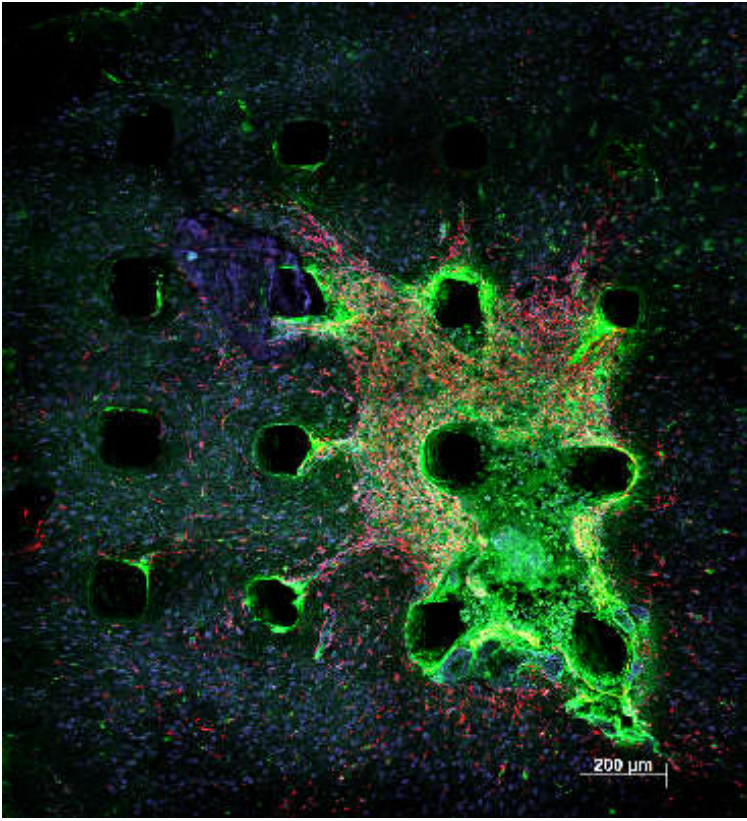


Figure 23: Intra-array electrode variability. Expression of CD68 (green) and GFAP (red) were highly concentrated in one section of the array in the lower right.

## **CHAPTER 4**

### **CONCLUSION**

Our exploration into the chronic implantation of Utah Electrode Arrays has shown us some of the many difficulties in understanding the performance of intracortical electrodes. There exists a broad host of factors that influence device performance, coming from biological and material changes to the electrode-tissue interface. The confluence of these factors are difficult to separate with current analysis methods.

There are many methods of measuring elements of electrode performance, addressing particular characteristics such as charge transfer or recording action potentials. Changes to these characteristics can be the result of changes to the tissue, by the absence of neurons or dense structures of glial cells encapsulating the device creating a resistive layer. Alternatively, damage to encapsulation integrity of the device would alter the flow of current passing through the electrode. In our study we reported on the chronic behavior of spontaneous local field potentials (LFPs) in the rat motor cortex, looking to better understand their relationship with other electrode characteristics. LFPs are low-frequency oscillations in neural signal that arise in the brain as a result of ensembles of neural firing and ionic changes. These signals have been successfully applied towards controlling brain-computer interfaces (BCIs) as an alternative to single-unit or multi-unit-based decoders. Single-unit and multi-unit analysis relies on discriminating high-frequency, low-amplitude spikes from wide band neural recordings, and are the most commonly used method of quantifying electrode performance and signal source for applications. LFPs have the advantage in having a significantly higher amplitude, and being less reliant on spike-recognition algorithms. In the absence of evoked behavior, units can be

unreliable, appearing and disappearing or changing between experiments. In our experiments, we analyzed trends in the LFP bandpower from 0.1-100 Hz over 26 weeks, recording from lightly anesthetized rats. We found that bandpower was correlated with overall trends in single unit activity detected. The connections between low-frequency LFPs and high-frequency units are not well understood, and will require better understanding of the frequency-dependent behavior of neural tissue and circuits.

The biological response to implanted electrodes is a major hurdle in understanding the chronic performance of neural devices. Many avenues of device design have attempted to address the biocompatibility of intracortical devices, utilizing unique geometries and materials to minimize the immune response. We looked at one such unique device, the Utah electrode array, which is currently used in human trials of BCIs for restoring function to paralyzed patients, and amorphous silicon carbide (a-SiC), a promising material for neural devices due to its low reactivity and favorable electrical properties. We compared a-SiC against a conventional material for biological implants, Parylene-C, which has an established history of being well-tolerated by the body. Implanting 4x4 UEAs coated with either material, as well as uncoated silicon arrays, in the cortex of rats, we discovered the response of a-SiC was heightened beyond 60 days post-implant. Parylene-C consistently performed better at all three sacrifice points (60, 90, 120 days), showing greater neuron density and reduced reactive astrocyte and activated microglia presence. The gross histological changes caused by UEA implants suggest the array geometry is not extremely well-suited for use in rat. We frequently observed large lesions extending as deep as 0.5mm (half the length of the array) in the surface of the brain beneath the array, containing collagenous tissue and glial cells. These lesions may have been caused by distortion during

implantation, or extensive activity by fibroblasts or glia. Besides causing uneven depth of implantation for individual electrodes, the absence of tissue caused by the lesion made it difficult to quantify the immune response at shallow depths and compare to other studies in literature.

## REFERENCES

- [1] National Spinal Cord Injury Statistical Center, “Facts and Figures at a Glance. Birmingham, AL: University of Alabama at Birmingham, 2016.”
- [2] M. S. Soichet, C. C. Tate, M. D. Baumann, and M. C. LaPlaca, “Strategies for Regeneration and Repair in the Injured Central Nervous System,” *Indwelling Neural Implant.*, 2008.
- [3] E. Biddiss and T. Chau, “Upper-limb prosthetics: Critical factors in device abandonment,” *Am. J. Phys. Med. Rehabil.*, 2007.
- [4] L. Whelan and N. Wagner, “Analysis of Factors Influencing Outcomes of Full and Partial Hand Multi-articulating Prostheses,” *J. Hand Ther.*, 2016.
- [5] J. Z. Laferrier, L. V. McFarland, M. L. Boninger, R. A. Cooper, and G. E. Reiber, “Wheeled mobility: Factors influencing mobility and assistive technology in veterans and servicemembers with major traumatic limb loss from Vietnam war and OIF/OEF conflicts,” *J. Rehabil. Res. Dev.*, 2010.
- [6] J. D. R. Millán et al., “Combining brain-computer interfaces and assistive technologies: State-of-the-art and challenges,” *Frontiers in Neuroscience*. 2010.
- [7] S. I. Ryu and K. V. Shenoy, “Human cortical prostheses: lost in translation?,” *Neurosurg. Focus*, 2009.
- [8] M. D. Serruya, N. G. Hatsopoulos, L. Paninski, M. R. Fellows, and J. P. Donoghue, “Instant neural control of a movement signal,” *Nature*, 2002.
- [9] D. M. Taylor, S. I. Tillery, and A. B. Schwartz, “Direct cortical control of 3D neuroprosthetic devices,” *Science (80-. )*, 2002.
- [10] J. M. Carmena et al., “Learning to control a brain-machine interface for reaching and grasping by primates,” *PLoS Biol.*, 2003.
- [11] M. Velliste, S. Perel, M. C. Spalding, a S. Whitford, and a B. Schwartz, “Cortical control of a robotic arm for self-feeding,” *Nature*, 2008.
- [12] L. Shpigelman, H. Lalazar, and E. Vaadia, “Kernel-ARMA for Hand Tracking and Brain-Machine Interfacing During 3D Motor Control,” *Neural Inf. Process. Syst.*, 2008.
- [13] K. Ganguly and J. M. Carmena, “Emergence of a stable cortical map for neuroprosthetic control,” *PLoS Biol.*, 2009.

- [14] A. J. Suminski, D. C. Tkach, A. H. Fagg, and N. G. Hatsopoulos, "Incorporating Feedback from Multiple Sensory Modalities Enhances Brain-Machine Interface Control," *J. Neurosci.*, 2010.
- [15] L. R. Hochberg et al., "Reach and grasp by people with tetraplegia using a neurally controlled robotic arm," *Nature*, vol. 485, no. 7398, pp. 372–375, May 2012.
- [16] J. D. Simeral, S.-P. Kim, M. J. Black, J. P. Donoghue, and L. R. Hochberg, "Neural control of cursor trajectory and click by a human with tetraplegia 1000 days after implant of an intracortical microelectrode array," *J. Neural Eng.*, vol. 8, no. 2, p. 025027, Apr. 2011.
- [17] L. R. Hochberg et al., "Neuronal ensemble control of prosthetic devices by a human with tetraplegia," *Nature*, vol. 442, no. 7099, pp. 164–171, 2006.
- [18] S. P. Kim, J. D. Simeral, L. R. Hochberg, J. P. Donoghue, and M. J. Black, "Neural control of computer cursor velocity by decoding motor cortical spiking activity in humans with tetraplegia," *J. Neural Eng.*, 2008.
- [19] J. S. Brumberg, A. Nieto-Castanon, P. R. Kennedy, and F. H. Guenther, "Brain-computer interfaces for speech communication," *Speech Commun.*, vol. 52, no. 4, pp. 367–379, 2010.
- [20] T. Milekovic, A. A. Sarma, D. Bacher, J. D. Simeral, J. Saab, and C. Pandarinath, "Stable long - term BCI - enabled communication in ALS and locked - in syndrome using LFP signals," 2018.
- [21] R. A. Green, N. H. Lovell, G. G. Wallace, and L. A. Poole-Warren, "Conducting polymers for neural interfaces: Challenges in developing an effective long-term implant," *Biomaterials*, 2008.
- [22] M. Jorfi, J. L. Skousen, C. Weder, and J. R. Capadona, "Progress towards biocompatible intracortical microelectrodes for neural interfacing applications," *J. Neural Eng.*, vol. 12, no. 1, 2015.
- [23] N. Chou, S. Yoo, and S. Kim, "A largely deformable surface type neural electrode array based on PDMS," *IEEE Trans. Neural Syst. Rehabil. Eng.*, 2013.
- [24] D. Khodagholy et al., "NeuroGrid: Recording action potentials from the surface of the brain," *Nat. Neurosci.*, 2015.
- [25] A. Sharma et al., "Long term in vitro functional stability and recording longevity of fully integrated wireless neural interfaces based on the Utah Slant Electrode Array," in *Journal of Neural Engineering*, 2011.

- [26] J. P. Roche and M. R. Hansen, "On the Horizon: Cochlear Implant Technology," *Otolaryngologic Clinics of North America*. 2015.
- [27] D. M. Brandman, S. S. Cash, and L. R. Hochberg, "Review: Human Intracortical Recording and Neural Decoding for Brain-Computer Interfaces," *IEEE Transactions on Neural Systems and Rehabilitation Engineering*. 2017.
- [28] E. M. Maynard, C. T. Nordhausen, and R. A. Normann, "The Utah Intracortical Electrode Array: A recording structure for potential brain-computer interfaces," *Electroencephalogr. Clin. Neurophysiol.*, 1997.
- [29] P. J. Rousche and R. A. Normann, "Chronic intracortical microstimulation (ICMS) of cat sensory cortex using the utah intracortical electrode array," *IEEE Trans. Rehabil. Eng.*, vol. 7, no. 1, pp. 56–68, Mar. 1999.
- [30] G. H. Mulliken, S. Musallam, and R. A. Andersen, "Decoding Trajectories from Posterior Parietal Cortex Ensembles," *J. Neurosci.*, 2008.
- [31] C. A. Chestek et al., "Long-term stability of neural prosthetic control signals from silicon cortical arrays in rhesus macaque motor cortex," in *Journal of Neural Engineering*, 2011.
- [32] R. D. Flint, Z. A. Wright, M. R. Scheid, and M. W. Slutzky, "Long term, stable brain machine interface performance using local field potentials and multiunit spikes," *J. Neural Eng.*, vol. 10, no. 5, 2013.
- [33] H. A. C. Wark et al., "A new high-density (25 electrodes/mm<sup>2</sup>) penetrating microelectrode array for recording and stimulating sub-millimeter neuroanatomical structures," *J. Neural Eng.*, 2013.
- [34] E. M. Maynard, E. Fernandez, and R. A. Normann, "A technique to prevent dural adhesions to chronically implanted microelectrode arrays," *J. Neurosci. Methods*, vol. 97, no. 2, pp. 93–101, 2000.
- [35] P. J. Rousche and R. A. Normann, "A method for pneumatically inserting an array of penetrating electrodes into cortical tissue," *Ann. Biomed. Eng.*, 1992.
- [36] S. Suner, M. R. Fellows, C. Vargas-Irwin, G. K. Nakata, and J. P. Donoghue, "Reliability of signals from a chronically implanted, silicon-based electrode array in non-human primate primary motor cortex," *IEEE Trans. Neural Syst. Rehabil. Eng.*, vol. 13, no. 4, pp. 524–541, 2005.
- [37] A. S. Dickey, A. Suminski, Y. Amit, and N. G. Hatsopoulos, "Single-Unit Stability Using Chronically Implanted Multielectrode Arrays," *J. Neurophysiol.*, vol. 102, no. 2, pp. 1331–1339, 2009.



- [38] C. M. Gray, P. E. Maldonado, M. Wilson, and B. McNaughton, "Tetrodes markedly improve the reliability and yield of multiple single-unit isolation from multi-unit recordings in cat striate cortex," *J. Neurosci. Methods*, vol. 63, no. 1–2, pp. 43–54, 1995.
- [39] Y. Kajikawa and C. E. Schroeder, "How local is the local field potential?," *Neuron*, vol. 72, no. 5, pp. 847–858, Dec. 2011.
- [40] A. Jackson and T. M. Hall, "Decoding Local Field Potentials for Neural Interfaces," *IEEE Trans. Neural Syst. Rehabil. Eng.*, vol. 25, no. 10, pp. 1705–1714, 2017.
- [41] J. C. Barrese, J. Aceros, and J. P. Donoghue, "Scanning electron microscopy of chronically implanted intracortical microelectrode arrays in non-human primates.," *J Neural Eng*, vol. 13, no. 2, p. 26003, 2016.
- [42] J. L. Collinger et al., "High-performance neuroprosthetic control by an individual with tetraplegia," *Lancet*, 2013.
- [43] A. B. Schwartz, X. T. Cui, D. J. J. Weber, and D. W. Moran, "Brain-Controlled Interfaces: Movement Restoration with Neural Prosthetics," *Neuron*. 2006.
- [44] M. A. M. Freire et al., "Comprehensive analysis of tissue preservation and recording quality from chronic multielectrode implants," *PLoS One*, 2011.
- [45] P. N. Sergi, W. Jensen, and K. Yoshida, "Interactions among biotic and abiotic factors affect the reliability of tungsten microneedles puncturing in vitro and in vivo peripheral nerves: A hybrid computational approach," *Mater. Sci. Eng. C*, vol. 59, pp. 1089–1099, 2016.
- [46] A. Prasad et al., "Abiotic-biotic characterization of Pt/Ir microelectrode arrays in chronic implants," *Front. Neuroeng.*, vol. 7, no. February, pp. 1–15, 2014.
- [47] A. Prasad et al., "Comprehensive characterization and failure modes of tungsten microwire arrays in chronic neural implants," *J. Neural Eng.*, vol. 9, no. 5, p. 056015, 2012.
- [48] A. Prasad et al., "Coupling biotic and abiotic metrics to create a testbed for predicting neural electrode performance," in *Proceedings of the Annual International Conference of the IEEE Engineering in Medicine and Biology Society, EMBS*, 2011, pp. 3020–3023.
- [49] T. D. Y. Kozai, A. S. Jaquins-Gerstl, A. L. Vazquez, A. C. Michael, and X. T. Cui, "Brain tissue responses to neural implants impact signal sensitivity and intervention strategies," *ACS Chem. Neurosci.*, vol. 6, no. 1, pp. 48–67, Jan. 2015.
- [50] V. S. Polikov, P. A. Tresco, and W. M. Reichert, "Response of brain tissue to chronically implanted neural electrodes," *J. Neurosci. Methods*, vol. 148, no. 1, pp. 1–18, Oct. 2005.

- [51] J. C. Barrese et al., “Failure mode analysis of silicon-based intracortical microelectrode arrays in non-human primates,” *J. Neural Eng.*, 2013.
- [52] S. . Malhotra, Z. . Rek, S. . Yalisove, and J. . Bilello, “Analysis of thin film stress measurement techniques,” *Thin Solid Films*, 1997.
- [53] J. C. Williams, J. A. Hippensteel, J. Dilgen, W. Shain, and D. R. Kipke, “Complex impedance spectroscopy for monitoring tissue responses to inserted neural implants,” *J. Neural Eng.*, vol. 4, no. 4, pp. 410–423, 2007.
- [54] G. C. McConnell, H. D. Rees, A. I. Levey, C.-A. A. Gutekunst, R. E. Gross, and R. V. Bellamkonda, “Implanted neural electrodes cause chronic, local inflammation that is correlated with local neurodegeneration,” *J. Neural Eng.*, vol. 6, no. 5, p. 056003, 2009.
- [55] J. M. Hsu, L. Rieth, R. A. Normann, P. Tathireddy, and F. Solzbacher, “Encapsulation of an integrated neural interface device with parylene C,” *IEEE Trans. Biomed. Eng.*, 2009.
- [56] F. Deku, Y. Cohen, A. Joshi-Imre, A. Kanneganti, T. Gardner, and S. Cogan, “Amorphous silicon carbide ultramicroelectrode arrays for neural stimulation and recording,” *J. Neural Eng.*, 2017.
- [57] S. E. Sadow, *Silicon Carbide Biotechnology: A Biocompatible Semiconductor for Advanced Biomedical Devices and Applications: Second Edition*. 2016.
- [58] G. L. Knaack et al., “In vivo Characterization of Amorphous Silicon Carbide As a Biomaterial for Chronic Neural Interfaces,” *Front. Neurosci.*, vol. 10, 2016.
- [59] N. F. Nolta, M. B. Christensen, P. D. Crane, J. L. Skousen, and P. A. Tresco, “BBB leakage, astrogliosis, and tissue loss correlate with silicon microelectrode array recording performance,” *Biomaterials*, vol. 53, pp. 753–762, 2015.
- [60] B. D. Winslow, M. B. Christensen, W. K. Yang, F. Solzbacher, and P. A. Tresco, “A comparison of the tissue response to chronically implanted Parylene-C-coated and uncoated planar silicon microelectrode arrays in rat cortex,” *Biomaterials*, vol. 31, no. 35, pp. 9163–9172, 2010.
- [61] B. Black et al., “Chronic recording and electrochemical performance of Utah microelectrode arrays implanted in rat motor cortex,” *J Neurophysiol.*, 2018.
- [62] J. R. Wolpaw, N. Birbaumer, D. J. McFarland, G. Pfurtscheller, and T. M. Vaughan, “Brain-computer interfaces for communication and control,” *Clin. Neurophysiol.*, vol. 113, no. 6, pp. 767–91, 2002.

- [63] S. Makeig, C. Kothe, T. Mullen, N. Bigdely-Shamlo, Z. Zhang, and K. Kreutz-Delgado, “Evolving signal processing for brain-computer interfaces,” in *Proceedings of the IEEE*, 2012, vol. 100, no. SPL CONTENT, pp. 1567–1584.
- [64] J. J. Vidal, “Toward Direct Brain-Computer Communication,” *Annu. Rev. Biophys. Bioeng.*, vol. 2, no. 1, pp. 157–180, 1973.
- [65] J. J. Vidal, “Realtime Detection of Brain Events in EEG,” *Proc. IEEE*, vol. 65, no. 5, pp. 633–641, 1977.
- [66] G. Pfurtscheller, C. Guger, G. Müller, G. Krausz, and C. Neuper, “Brain oscillations control hand orthosis in a tetraplegic,” *Neurosci. Lett.*, 2000.
- [67] R. Ortner, B. Z. Allison, G. Korisek, H. Gaggl, and G. Pfurtscheller, “An SSVEP BCI to control a hand orthosis for persons with tetraplegia,” *IEEE Trans. Neural Syst. Rehabil. Eng.*, 2011.
- [68] E. C. Leuthardt, G. Schalk, J. R. Wolpaw, J. G. Ojemann, and D. W. Moran, “A brain-computer interface using electrocorticographic signals in humans,” *J. Neural Eng.*, vol. 1, no. 2, pp. 63–71, 2004.
- [69] G. Schalk and E. C. Leuthardt, “Brain-computer interfaces using electrocorticographic signals,” *IEEE Rev. Biomed. Eng.*, 2011.
- [70] M. A. Lebedev and M. A. L. Nicolelis, “Brain-machine interfaces: past, present and future,” *Trends Neurosci.*, vol. 29, no. 9, pp. 536–546, 2006.
- [71] G. Santhanam, S. I. Ryu, B. M. Yu, A. Afshar, and K. V. Shenoy, “A high-performance brain-computer interface,” *Nature*, vol. 442, no. 7099, pp. 195–198, 2006.
- [72] T. D. Y. Y. Kozai et al., “Comprehensive chronic laminar single-unit, multi-unit, and local field potential recording performance with planar single shank electrode arrays,” *J. Neurosci. Methods*, vol. 242, pp. 15–40, 2015.
- [73] S. N. Baker et al., “Multiple single unit recording in the cortex of monkeys using independently moveable microelectrodes,” in *Journal of Neuroscience Methods*, 1999, vol. 94, no. 1, pp. 5–17.
- [74] S. Perel et al., “Single-unit activity, threshold crossings, and local field potentials in motor cortex differentially encode reach kinematics,” *J. Neurophysiol.*, vol. 114, no. 3, pp. 1500–1512, 2015.
- [75] A. Jackson and E. E. Fetz, “Compact Movable Microwire Array for Long-Term Chronic Unit Recording in Cerebral Cortex of Primates,” *J. Neurophysiol.*, vol. 98, no. 5, pp. 3109–3118, 2007.

- [76] P. R. Kennedy and R. A. E. Bakay, "Restoration of neural output from a paralyzed patient by a direct brain connection," *Neuroreport*, vol. 9, no. 8, pp. 1707–1711, 1998.
- [77] P. R. Kennedy, R. A. E. Bakay, M. M. Moore, K. Adams, and J. Goldwaithe, "Direct control of a computer from the human central nervous system," *IEEE Trans. Rehabil. Eng.*, 2000.
- [78] P. R. Kennedy, M. T. Kirby, M. M. Moore, B. King, and A. Mallory, "Computer control using human intracortical local field potentials.," *IEEE Trans. Neural Syst. Rehabil. Eng.*, 2004.
- [79] D. P. McMullen et al., "Demonstration of a semi-autonomous hybrid brain-machine interface using human intracranial EEG, eye tracking, and computer vision to control a robotic upper limb prosthetic," *IEEE Trans. Neural Syst. Rehabil. Eng.*, vol. 22, no. 4, pp. 784–796, 2014.
- [80] A. Branner, R. B. Stein, E. Fernandez, Y. Aoyagi, and R. A. Normann, "Long-Term Stimulation and Recording with a Penetrating Microelectrode Array in Cat Sciatic Nerve," *IEEE Trans. Biomed. Eng.*, 2004.
- [81] S. J. Hanrahan et al., "The Effects of Propofol on Local Field Potential Spectra, Action Potential Firing Rate, and Their Temporal Relationship in Humans and Felines," *Front. Hum. Neurosci.*, vol. 7, no. April, pp. 1–11, 2013.
- [82] A. Silva, H. Cardoso-Cruz, F. Silva, V. Galhardo, and L. Antunes, "Comparison of anesthetic depth indexes based on thalamocortical local field potentials in rats," *Anesthesiology*, vol. 112, no. 2, pp. 355–363, 2010.
- [83] M. Kreuzer, H. Hentschke, B. Antkowiak, C. Schwarz, E. F. Kochs, and G. Schneider, "Cross-approximate entropy of cortical local field potentials quantifies effects of anesthesia--a pilot study in rats.," *BMC Neurosci.*, vol. 11, no. 1, p. 122, 2010.
- [84] O. Herreras, "Local Field Potentials: Myths and Misunderstandings," *Front. Neural Circuits*, 2016.
- [85] S. Ray, N. E. Crone, E. Niebur, P. J. Franaszczuk, and S. S. Hsiao, "Neural Correlates of High-Gamma Oscillations (60-200 Hz) in Macaque Local Field Potentials and Their Potential Implications in Electrocorticography," *J. Neurosci.*, vol. 28, no. 45, pp. 11526–11536, 2008.
- [86] P. E. Greenwood, M. D. McDonnell, and L. M. Ward, "Dynamics of gamma bursts in local field potentials," *Neural Computation*, vol. 27, no. 1, pp. 74–103, 2015.

- [87] S. Salelkar, G. M. Somasekhar, S. Ray, A. S. Salelkar, G. M. Somasekhar, and S. Ray, “Distinct frequency bands in the local field potential are differently tuned to stimulus drift rate.,” *J. Neurophysiol.*, 2018.
- [88] P. L. Nunez, *Neocortical Dynamics and Human EEG Rhythms*. 1995.
- [89] M. Denker, “The Local Field Potential Reflects Surplus Spike Synchronicity,” *Cereb Cortex*, no. Dec, 2011.
- [90] M. Hu, M. Li, W. Li, and H. Liang, “Joint analysis of spikes and local field potentials using copula,” *Neuroimage*, vol. 133, pp. 457–467, 2016.
- [91] S. Waldert, R. N. Lemon, and A. Kraskov, “Influence of spiking activity on cortical local field potentials,” *J. Physiol.*, 2013.
- [92] A. K. Bansul, C. E. Vargas-Irwin, W. Truccolor, and J. P. Donoghue, “Relationships among low-frequency LFPs, spiking activity, and 3D reach and grasp kinematics in MI and PMv,” *J Neurophysiol.*, 2011.
- [93] M. J. Rasch, A. Gretton, Y. Murayama, W. Maass, and N. K. Logothetis, “Inferring Spike Trains From Local Field Potentials,” *J. Neurophysiol.*, vol. 99, no. 3, pp. 1461–1476, Mar. 2008.
- [94] F. Cortese et al., “Abnormal local field potentials precede clinical complications after DBS surgery for Parkinson’s disease: A case report,” *Clin. Neurophysiol.*, vol. 126, no. 5, pp. 1056–1058, 2015.
- [95] M. Rosa et al., “Time dependent subthalamic local field potential changes after DBS surgery in Parkinson’s disease,” *Exp. Neurol.*, vol. 222, no. 2, pp. 184–190, 2010.
- [96] J. A. Thompson, D. Lanctin, N. F. Ince, and A. Abosch, “Clinical implications of local field potentials for understanding and treating movement disorders,” *Stereotactic and Functional Neurosurgery*, vol. 92, no. 4. pp. 251–263, 2014.
- [97] A. J. Fenoy and R. K. Simpson, “Risks of common complications in deep brain stimulation surgery: management and avoidance,” *J. Neurosurg.*, 2014.
- [98] A. Priori, G. Foffani, L. Rossi, and S. Marceglia, “Adaptive deep brain stimulation (aDBS) controlled by local field potential oscillations,” *Experimental Neurology*. 2013.
- [99] A. Bashashati, M. Fatourehchi, R. K. Ward, and G. E. Birch, “A survey of signal processing algorithms in brain-computer interfaces based on electrical brain signals,” *Journal of Neural Engineering*. 2007.

- [100] M. R. Scheid, R. D. Flint, Z. A. Wright, M. W. Slutzky, and S. Member, "Long-Term , Stable Behavior of Local Field Potentials During Brain Machine Interface Use," pp. 307–310, 2013.
- [101] S. F. Cogan, P. R. Troyk, J. Ehrlich, C. M. Gasbarro, and T. D. Plante, "The influence of electrolyte composition on the in vitro charge-injection limits of activated iridium oxide (AIROF) stimulation electrodes," *J. Neural Eng.*, 2007.
- [102] S. F. Cogan, P. R. Troyk, J. Ehrlich, and T. D. Plante, "In vitro comparison of the charge-injection limits of activated iridium oxide (AIROF) and platinum-indium microelectrodes," *IEEE Trans. Biomed. Eng.*, 2005.
- [103] J. Csicsvari et al., "Massively Parallel Recording of Unit and Local Field Potentials With Silicon- Based Electrodes '," *J. Neurophysiol.*, vol. 90, no. 2, pp. 1314–1323, 2003.
- [104] T. Milekovic et al., "Stable long-term BCI-enabled communication in ALS and locked-in syndrome using LFP signals," *J. Neurophysiol.*, 2018.
- [105] K. van Kuyck, M. Welkenhuysen, L. Arckens, R. Sciot, and B. Nuttin, "Histological alterations induced by electrode implantation and electrical stimulation in the human brain: a review.," *Neuromodulation*, 2007.
- [106] W. Grill, "Signal considerations for chronically implanted electrodes for brain interfacing," *Indwelling Neural Implant. Strateg. Contend. ...*, 2008.
- [107] D. R. Kipke et al., "Advanced Neurotechnologies for Chronic Neural Interfaces: New Horizons and Clinical Opportunities," *J. Neurosci.*, vol. 28, no. 46, pp. 11830–11838, Nov. 2008.
- [108] W. Shain et al., "Controlling cellular reactive responses around neural prosthetic devices using peripheral and local intervention strategies," *IEEE Trans. Neural Syst. Rehabil. Eng.*, vol. 11, no. 2, pp. 186–188, 2003.
- [109] K. Nakajima, S. Honda, Y. Tohyama, Y. Imai, S. Kohsaka, and T. Kurihara, "Neurotrophin secretion from cultured microglia," *J. Neurosci. Res.*, 2001.
- [110] K. Sutherland, J. R. Mahoney, A. J. Coury, and J. W. Eaton, "Degradation of biomaterials by phagocyte-derived oxidants," *J. Clin. Invest.*, 1993.
- [111] D. H. Szarowski et al., "Brain responses to micro-machined silicon devices," *Brain Res.*, 2003.
- [112] D. J. Edell, V. Van Toi, V. M. McNeil, and L. D. Clark, "Factors Influencing the Biocompatibility of Insertable Silicon Microshafts in Cerebral Cortex," *IEEE Trans. Biomed. Eng.*, 1992.

- [113] S. F. Cogan, D. J. Edell, A. A. Guzelian, Y. P. Liu, and R. Edell, "Plasma-enhanced chemical vapor deposited silicon carbide as an implantable dielectric coating," *J. Biomed. Mater. Res. - Part A*, 2003.
- [114] C. Hansi, A. Arab, A. Rzany, I. Ahrens, C. Bode, and C. Hehrlein, "Differences of platelet adhesion and thrombus activation on amorphous silicon carbide, magnesium alloy, stainless steel, and cobalt chromium stent surfaces," *Catheterization and Cardiovascular Interventions*. 2009.
- [115] J. M. Hsu, P. Tathireddy, L. Rieth, A. R. Normann, and F. Solzbacher, "Characterization of a-SiC<sub>x</sub>:H thin films as an encapsulation material for integrated silicon based neural interface devices," *Thin Solid Films*, 2007.
- [116] M. Goss-Varley et al., "Microelectrode implantation in motor cortex causes fine motor deficit: Implications on potential considerations to Brain Computer Interfacing and Human Augmentation," *Sci. Rep.*, vol. 7, no. 1, pp. 1–12, 2017.

## **BIOGRAPHICAL SKETCH**

Ellen Shih hails from Plano, Texas, and graduated from the Texas Academy of Math and Science (TAMS) at the University of North Texas in 2013. Ellen was awarded the Academic Excellence Scholarship to attend The University of Texas at Dallas and received a Bachelor of Science in Biomedical Engineering in 2016, continuing into a master's degree through the Fast-Track program. She began working in the Neural Interfaces Laboratory in 2015 and remained to complete her graduate thesis work.



## CURRICULUM VITAE

### Ellen Shih

---

[exs125130@utdallas.edu](mailto:exs125130@utdallas.edu) ☐ 1506 N Waterview Drive

M: (214)-449-6281 ☐ Richardson, TX 75080

#### Education

M.S. in Biomedical Engineering

University of Texas at Dallas (UTD); December 2018

B.S. in Biomedical Engineering

University of Texas at Dallas (UTD); May 2016

Academic Excellence Scholarship recipient

#### Academic Work

##### **Master's Thesis: Fall 2016 – Summer 2018**

Comparative performance of conventional parylene-coated Blackrock microelectrode arrays to those with amorphous silicon carbide encapsulation using immunohistochemical analysis. Performed surgical procedures and post-operative care on animals following university IACUC protocols. Signal analysis of neural recording data to analyze device performance.

##### **Undergraduate Capstone: Developing a Library of Cleft Lip and Palate Models, Fall 2015 - Spring 2016**

Developed a series of 3D-printed models derived from CT and surface imaging to illustrate range of cleft lip and palate conditions for patient education at Children's Medical Center Dallas as a team-based Senior Capstone project. Work published in the Cleft Palate-Craniofacial Journal under Dr. Pang-Yun Chou and Dr. Alex Kane of UTSW.

#### Technical Experience

- Microsoft Office, Adobe Photoshop, Illustrator, InDesign
- C++, Labview, Matlab
- Materialise Mimics, 3-Matics, Solidworks

#### Languages

- Native English speaker
- Conversational Mandarin Chinese and Spanish